Title

Bruce suppresses autophagy-regulated caspase activity and wing tissue growth in *Drosophila*

Authors

Natsuki Shinoda[a,1], Yutaro Hama[b], Nozomi Hanawa[a] and Masayuki Miura[a,c,1]

Affiliations & Footnotes

[a]Department of Genetics, Graduate School of Pharmaceutical Sciences, The University of Tokyo, 7-3-1 Hongo, Bunkyo-ku, Tokyo 113-0033, Japan

[b]Institute for Genetic Medicine, Hokkaido University, Kita 15, Nishi 7, Kita-ku, Sapporo, Hokkaido, 060-0815, Japan

[c]Laboratory for Cell Vigor Regulation, National Institute for Basic Biology, Nishigonaka 38, Myodaiji, Okazaki, Aichi 444-8585, Japan

[1]Corresponding authors

Corresponding Authors

Natsuki Shinoda: Department of Genetics, Graduate School of Pharmaceutical Sciences, University of Tokyo 7-3-1 Hongo, Bunkyo-ku, Tokyo 113-0033, Japan. Telephone: +81-3-5841-4863. E-mail: f-shinoda.natsuki@g.ecc.u-tokyo.ac.jp

Masayuki Miura: Laboratory for Cell Vigor Regulation, National Institute for Basic Biology, Nishigonaka 38, Myodaiji, Okazaki, Aichi 444-8585, Japan. Telephone: +81-564-55-7650. E-mail: miura@nibb.ac.jp

Abstract

Caspases are cysteine-aspartic proteases that mediate both lethal and non-lethal cellular outcomes, including the promotion of tissue growth. However, the mechanisms underlying the differential regulation of these activities remain unclear. We have previously shown that among the two *Drosophila* executioner caspases, Dcp-1 and Drice, Dcp-1 promotes tissue growth in a non-lethal manner, independent of canonical apoptotic signaling. Herein, we demonstrated that overexpressed Dcp-1, but not Drice, was activated without canonical apoptosome components. TurboID-based proximity labeling revealed distinct proximal proteomes, among which Sirtuin 1, an Atg8a deacetylase, which promotes autophagy, was specifically required for Dcp-1 activation. Autophagy-related genes, including Bcl-2 family members *Debcl* and *Buffy*, are required for Dcp-1 activation. Structure-based prediction using AlphaFold3 further identified Bruce, an autophagy-regulated inhibitor of apoptosis, as a Dcp-1-specific regulator acting outside the apoptosome-mediated pathway. Physiologically, Bruce suppresses wing tissue growth. These findings indicate that non-lethal Dcp-1 activity is governed by the autophagy-Bruce axis, enabling distinct non-lethal functions independent of cell death.

Keywords

Autophagy, Caspase, Drosophila, tissue growth, TurboID

43 **Introduction**

44 Caspases are cysteine-aspartic acid proteases that serve as the central executioners of apoptosis.
45 In *Drosophila*, core caspase-mediated signaling for apoptosis is well conserved (Nakajima &
46 Kuranaga, 2017; Shinoda & Miura, 2024). Upon apoptotic stimulation, the pro-apoptotic genes
47 *rpr*, *hid*, and *grim* (*RHG*), which antagonize DIAP-1, an inhibitor of apoptosis protein (IAP),
48 are transcriptionally upregulated. The degradation of DIAP-1 allows the initiator caspase Dronc
49 and its activator Dark to assemble into the apoptosome, thereby triggering a proteolytic cascade
50 that activates the executioner caspases Dcp-1 and Drice, ultimately leading to apoptosis. In
51 addition to their role in apoptosis, caspases perform diverse non-cell death functions
52 collectively termed caspase-dependent non-lethal cellular processes (Aram *et al*, 2017).
53 However, the mechanisms that differentially regulate lethal and non-lethal caspase activity
54 remain largely unknown.

55 Functional specificity appears to arise at the level of the executioner caspases. Of the
56 two executioner caspases in *Drosophila*, Drice is more potent than Dcp-1 in inducing cell death
57 in wing imaginal discs (Florentin & Arama, 2012). In contrast, Dcp-1 is required for autophagy
58 triggered by starvation or proteasome dysfunction in the ovaries (Hou *et al*, 2008; DeVorkin *et*
59 *al*, 2014; Choutka *et al*, 2017). We have previously demonstrated that Dcp-1, but not Drice,
60 specifically promotes imaginal tissue growth independent of apoptosome and cell death
61 (Shinoda *et al*, 2019). Mechanistically, we showed that cleavage-mediated inactivation of
62 Acinus, a positive regulator of autophagy (Nandi *et al*, 2014; Haberman *et al*, 2010), which
63 limits tissue growth independently of autophagy (Tyra *et al*, 2020), partly promotes tissue
64 growth (Shinoda *et al*, 2019). However, the upstream regulatory mechanisms that selectively
65 regulate Dcp-1 activity remain unknown.

66 Proximity labeling has emerged as a powerful approach for comprehensively analyzing
67 molecular interactions, including protein-protein interactions (Qin *et al*, 2021). TurboID

68 enables the rapid biotinylation of lysine residues on neighboring proteins within 10 minutes in
69 cultured cells (Branon *et al*, 2018). Streptavidin-based enrichment of these biotinylated proteins,
70 followed by mass spectrometry, allows the proteome-wide identification of proteins near a
71 target of interest. We previously generated *Drosophila* lines in which TurboID was knocked in
72 at the C-termini of Dronc, Dcp-1, or Drice (Shinoda *et al*, 2019). In wing imaginal discs,
73 TurboID-based labeling has revealed distinct proximity patterns for Dcp-1 and Drice,
74 suggesting that each executioner caspase is associated with a unique set of neighboring proteins
75 (Shinoda *et al*, 2019). We have shown that the differences in substrate specificity between Dcp-
76 1 and Drice were consistent with their distinct proximity profiles in the ovary, as exemplified
77 by BubR1 (Shinoda *et al*, 2023). Moreover, overexpression of *Fasciclin 3*, a Drice-proximal
78 protein identified in adult brains, induces non-lethal caspase activation in a Dronc-dependent
79 manner (Muramoto *et al*, 2025). These findings indicate that caspase-proximal proteins can
80 function not only as potential substrates but also as regulatory factors.
81 In this study, we investigated the regulatory mechanisms underlying Dcp-1 activation.
82 We found that the overexpression of *Dcp-1* induced a wingless phenotype. Using this
83 phenotype as a functional readout, we found that Dcp-1 activation specifically requires its
84 proximal protein Sirtuin 1 (Sirt1), Bcl-2 family members Debcl and Buffy, and components of
85 the autophagy pathway. Notably, the autophagy-regulated giant IAP Bruce specifically
86 interacts with and regulates Dcp-1 activity without affecting apoptosome-mediated core
87 apoptotic signaling, thereby suppressing wing imaginal tissue growth. Together, these findings
88 reveal that Bruce acts upstream to diverge the regulatory pathways of Dcp-1 and Drice, enabling
89 Dcp-1 to mediate distinct non-lethal functions through autophagy, independent of cell death.
90

Results

Overexpression of Dcp-1, but not Drice, induces apoptosis

Structurally, the executioner caspases, Dcp-1 and Drice, are similar, each comprising catalytic P20 and P10 domains and a highly disordered N-terminal prodomain (Fig. 1A). First, we assessed the ability of two executioner caspases to trigger apoptosis. Using the *WP-Gal4* driver, the overexpression of *Dcp-1* resulted in a wingless phenotype indicative of apoptotic cell death, whereas the overexpression of *Drice* did not (Fig. 1B), which is consistent with our previous observations in olfactory receptor neurons (Muramoto *et al*, 2025). Next, we examined the apoptotic potential of fluorescently tagged caspases in *Drosophila* S2 cells expressing mNeonGreen (mNG)-fused Dcp-1 or Drice. Dcp-1 expression caused a marked reduction in mNG intensity (Fig. EV1A–C) and a decreased number of mNG-positive cells (Fig. EV1A, D). These effects required Dcp-1 catalytic activity, as the mutation of the catalytic cysteine to glycine restored both mNG intensity and cell number (Fig. EV1A–D). In contrast, Drice expression neither reduced mNG intensity nor decreased the number of mNG-positive cells, resembling the catalytically inactive mutant (Fig EV1A–D). Taken together, these results demonstrate that Dcp-1, but not Drice, is activated upon overexpression and induces apoptosis in multiple cell types.

Dcp-1 activation is independent of the apoptosome composed of Dronc and Dark

Executioner caspases are typically activated by cleavage mediated by the initiator caspase, Dronc, which is activated through the assembly of the Dark-dependent apoptosome (Fig. 1C) (Nakajima & Kuranaga, 2017; Shinoda & Miura, 2024). We previously proposed that Dcp-1 can be activated independently of Dark and Dronc (Shinoda *et al*, 2019). To test this hypothesis further, we analyzed genetic modifiers of the Dcp-1-induced wingless phenotype. A heterozygous mutation in the *H99* deficiency, which encompasses the pro-apoptotic *reaper*, *hid*,

116 and *grim* (*RHG*) genes, rescued the wingless phenotype caused by *Dcp-1* overexpression (Fig.
117 1D, F). Similarly, expression of the caspase inhibitor *p35* or knockdown of *RHG* genes also
118 rescued this phenotype (Fig. 1E, F), suggesting that Dcp-1 induces apoptosis in a catalytic
119 activity-dependent manner under the control of RHG proteins. In contrast, knockdown of other
120 core apoptotic components, including Dark, Dronc, and Drice, or overexpression of the
121 dominant-negative form of Dronc ($Dronc^{DN}$) failed to suppress the wingless phenotype (Fig.
122 1E, F). These findings support our earlier observation that Dcp-1 can be activated independent
123 of the canonical apoptosome composed of Dronc and Dark to mediate non-lethal functions
124 (Shinoda *et al*, 2019). Collectively, these results indicate that, at least under overexpression
125 conditions, Dcp-1 activation proceeds independently of the apoptosome, in contrast to that of
126 Drice.
127
128 ***Dcp-1 and Drice show distinct expression patterns among tissues***
129 Proximal proteins of caspases have emerged as potential regulators of executioner caspase
130 activity (Muramoto *et al*, 2025). We have previously demonstrated that the proximal protein
131 patterns of Dcp-1 and Drice differ even within the same tissue, such as wing imaginal discs
132 (Shinoda *et al*, 2019). Based on this, we sought to identify Dcp-1-specific regulatory factors
133 among its proximal proteins. First, we examined the tissue distribution of *Drosophila* caspases
134 using previously established *Caspase::V5::TurboID* knock-in fly lines (Shinoda *et al*, 2019).
135 Expression patterns were analyzed in larval tissues, including the salivary glands, fat bodies,
136 and brain (Fig. EV2A), with confirmed expression in wing imaginal discs (Fig. 2A) as well as
137 in adult tissues, including the thorax, ovary, and testis (Fig. EV2B). Drice was ubiquitously
138 expressed in all examined tissues. In contrast, Dcp-1 expression was restricted to the larval
139 brain and adult ovaries and testes.
140

141 ***Drosophila executioner caspases associate with distinct sets of proximal proteins***

142 Next, we compared the proximal protein profiles of *Drosophila* executioner caspases, based on
143 our previous observation that Dcp-1 and Drice are associated with distinct sets of proximal
144 proteins, potentially reflecting differences in their activation mechanisms (Shinoda *et al*, 2019).
145 Streptavidin staining, used to visualize proteins biotinylated via TurboID-mediated proximity
146 labeling, revealed distinct patterns of Dcp-1 and Drice expression across tissues (Figs. 2A and
147 EV2A, B). To directly compare their proximal landscapes in the same cellular context, we
148 focused on the imaginal discs. NeutrAvidin-based purification of biotinylated proteins,
149 followed by mass spectrometry, identified 818 proteins (Fig. 2B, C). As expected, the proximal
150 proteomes of Dcp-1 and Drice were distinct. BubR1 and Fasciclin 3 isoform G, previously
151 identified as Drice-proximal in adult brain and ovary tissues (Shinoda *et al*, 2023; Muramoto
152 *et al*, 2025), were enriched in the Drice-associated proteome (Fig. 2C, Table EV1), suggesting
153 that Drice maintains its proximity to specific partners across tissues. Among the top Dcp-1-
154 enriched proximal proteins was the chaperonin containing TCP1 subunit 8 (CCT8). To validate
155 these findings, we generated an antibody against CCT8 (Fig. 2D). Western blotting confirmed
156 the presence of CCT8 in Dcp-1::V5::TurboID samples but not in Drice::V5::TurboID samples
157 (Fig. 2E). Taken together, these results show that, even when expressed at comparable levels
158 in the same tissue, Dcp-1 and Drice are associated with distinct sets of proximal proteins, which
159 is consistent with their differential regulation and functional specificity.

160

161 ***Screening of Dcp-1 proximal proteins identifies Sirt1 as a Dcp-1-specific activator***

162 To identify potential regulators of Dcp-1 activation, we performed an RNAi screen targeting
163 eight genes that were selectively proximal to Dcp-1 relative to Drice and wild-type controls
164 (Dcp-1/Drice fold change > 1.5, Dcp-1/Control fold change > 10 and PSM ≧ 2; Table EV1),
165 using two independent RNAi lines per gene (Fig. 2F). Under normal conditions, RNAi-

166 mediated knockdown of the chaperonin components *CCT2* and *CCT8* resulted in a wingless
167 phenotype, whereas knockdown of other genes had no effect (Fig. EV3A). Under *Dcp*-1
168 overexpression conditions, knockdown of *Fkbp59* or *Sirt1* partially suppressed Dcp-1-induced
169 cell death (Fig. 2G, Fig. EV3B). The requirement for Sirt1 was further confirmed using a
170 transheteroallelic combination of two previously described *Sirt1* deletion alleles, $Sirt1^{2A-7-11}$
171 (Xie & Golic, 2004; Furuyama *et al*, 2004) and $Sirt1^{4.5}$ (Newman *et al*, 2002), which
172 significantly rescued the wingless phenotype (Fig. 2H, I). These results indicate that the Dcp-
173 1-proximal protein Sirt1 is required for Dcp-1 activation upon overexpression.
174
175 ***Dcp-1 activation specifically depends on Debcl, Buffy, and autophagy***
176 Sirt1, also known as dSir2, is a lysine deacetylase that promotes the expression of autophagy-
177 related genes via Atg8a deacetylation under starvation (Jacomin *et al*, 2020). Multiple studies
178 have linked Dcp-1 to the regulation of autophagy. Dcp-1, together with the Bcl-2 family
179 proteins Debcl and Buffy, but not Drice, has been shown to be required for starvation-induced
180 autophagy in *Drosophila* l(2)mbn cells (Hou *et al*, 2008), and Dcp-1 is also required for
181 autophagy in the ovary (Hou *et al*, 2008; DeVorkin *et al*, 2014; Choutka *et al*, 2017). More
182 recently, the BH3-only protein Sayonara (Synr) was reported to induce Dcp-1-dependent cell
183 death, which is regulated by Debcl, Buffy, and autophagy (Ikegawa *et al*, 2023). In contrast, a
184 gain-of-function modifier screen revealed that autophagy antagonizes Dcp-1-induced cell death
185 (Kim *et al*, 2010) and that Dcp-1 suppresses autophagy through cleavage-mediated inactivation
186 of Acinus (Haberman *et al*, 2010; Nandi *et al*, 2014).
187 Based on these reports, we examined whether Synr, Debcl, Buffy, and core autophagy
188 components regulate Dcp-1 activation. Knockdown of *Synr* did not suppress Dcp-1-induced
189 cell death, whereas knockdown of *Debcl* or *Buffy* significantly rescued this wingless phenotype
190 (Fig. 3A, B). Similarly, knockdown of the autophagy-related genes *Atg2* and *Atg8a* suppressed

191 Dcp-1-induced cell death (Fig. 3A, B), indicating that Debcl, Buffy, and autophagy are required
192 for Dcp-1 activation. To assess the specificity of these regulators, we analyzed the eye ablation
193 phenotype caused by overexpression of *Hid*, which triggers apoptosis via canonical apoptotic
194 signaling. As expected, this phenotype was rescued by *p35* expression or knockdown of *RHG*
195 genes and partially suppressed by inhibition of the Dark-, Dronc-, and Drice-dependent
196 apoptosome pathways (Fig. 3C), confirming its dependence on canonical apoptosis (Fig. 1C).
197 In contrast, *Hid*-induced apoptosis was not rescued by RNAi against *Dcp-1* (Fig. 3C), nor by
198 knockdown of *Sirt1* or *Fkbp59* (Fig. 3D). Furthermore, knockdown of *Debcl*, *Buffy*, and
199 autophagy genes failed to rescue *Hid*-induced apoptosis (Fig. 3E). Taken together, these results
200 indicate that Sirt1, Debcl, Buffy, and autophagy components are not general regulators of
201 apoptosis but function as specific activators of Dcp-1.
202
203 ***Cleaved Dcp-1 specifically interacts with a giant-IAP Bruce***
204 Next, we examined the molecular link between autophagy and Dcp-1 activation. Caspase
205 activation is negatively regulated by IAPs. In *Drosophila*, DIAP1 suppresses caspase activity
206 through ubiquitination (Ditzel *et al*, 2008) (Fig. 1C). In addition to DIAP1, *Drosophila* has
207 another giant IAP, *Bruce*, which is degraded via autophagy during oogenesis (Nezis *et al*, 2010).
208 Bruce inhibits autophagy under nutrient-rich conditions (Hou *et al*, 2008), suggesting mutual
209 negative regulation of Bruce and autophagy. Bruce selectively inhibits *reaper*-induced cell
210 death, but not *hid*-induced apoptosis, suggesting a degree of pathway specificity (Domingues
211 & Ryoo, 2012). These observations led us to focus on Bruce as a potential selective regulator
212 of Dcp-1 activation.
213 The structure of human Bruce/BIRC6 has recently been resolved using cryo-electron
214 microscopy (Hunkeler *et al*, 2023; Ehrmann *et al*, 2023; Liu *et al*, 2024), revealing several
215 conserved domains: linker domain (LD), baculoviral IAP repeat (BIR), WD40, β-X1, β-X2,

216 carbohydrate-binding module (CBM), ubiquitin-like (UBL), and ubiquitin-conjugating (UBC)
217 (Fig. 4A). The BIR domain mediates interactions with ubiquitination substrates by recognizing
218 N-terminal IAP-binding motifs (IBMs) (Berthelet & Dubrez, 2013). The consensus IBM
219 sequence is defined as A(K/T/V/I)(P/A/E)(F/E/I/S/Y) (Vaux & Silke, 2005). We identified
220 IBM-like sequences at the N-termini of the P20 domains of both Dcp-1 and Drice (Fig. 4B, C).
221 To assess the potential interaction between Bruce and these caspases, we used AlphaFold3 to
222 predict the structure of the complexes between Bruce and the IBM-like motifs of Dcp-1 and
223 Drice (Abramson *et al*, 2024). Consistent with the known architecture of BIRC6, AlphaFold3
224 predicted that the BIR domain of Bruce interacts with LD, WD40, β-X1, and β-X2 domains
225 (Fig. EV4A, B). For structural prediction, we used a Bruce fragment spanning residues 1–1960,
226 including the BIR domain and its associated Zn^{2+}-binding site (Fig. 4A), and 15-residue
227 peptides from the Dcp-1 and Drice cleavage sites encompassing their IBM-like motifs (Fig. 4B,
228 C). The predicted structures revealed a high-confidence interaction between Dcp-1 and the
229 Bruce BIR domain. All five AlphaFold3 models showed confident pLDDT scores (70–90) for
230 the N-terminal residues of Dcp-1, corresponding to the IBM-like motif (Fig. 4D, F). The
231 predicted binding mode resembled the canonical BIR-IBM interaction observed in XIAP BIR3-
232 Smac (Wu *et al*, 2000) (Fig. EV4C). In contrast, although Drice appeared to bind to Bruce in
233 the predicted models, the pLDDT scores were consistently low (<70) across the interaction
234 interface, including the four N-terminal residues, indicating low confidence in the predicted
235 interaction (Fig. 4E, G).

236 To validate these predictions, we performed co-immunoprecipitation assays on
237 *Drosophila* S2 cells. We found that only the cleaved form of Dcp-1, which forms a head-to-tail
238 dimer composed of the P20 and P10 domains (Julien & Wells, 2017), and not the full-length
239 protein, interacted with the N-terminal BIR domain of Bruce following apoptosis induction (Fig.
240 4H). Conversely, neither the cleaved nor full-length forms of Drice showed detectable

241 interactions with the Bruce BIR domain (Fig. 4H), corroborating the AlphaFold3 predictions.
242 Taken together, these findings suggest that Bruce specifically suppresses activated Dcp-1 but
243 not Drice and serves as a branching point for a Dcp-1-specific, non-canonical regulatory
244 pathway.
245
246 ***Bruce is ubiquitously expressed in wing imaginal discs***
247 Bruce has been reported to function in oogenesis and spermatogenesis in the ovaries and testes,
248 respectively (Arama *et al*, 2003, 2007; Kaplan *et al*, 2010; Nezis *et al*, 2010; Hou *et al*, 2008).
249 However, its expression in other tissues has not been thoroughly characterized. To examine the
250 tissue distribution of Bruce, we generated CRISPR/Cas9-mediated knock-in flies in which an
251 mStayGold::C4 linker::V5-tag (Ando *et al*, 2024) was inserted into the N-terminus of Bruce
252 (Fig. EV5A). Using the knocked-in line, we confirmed that Bruce was expressed in the ovaries
253 (Fig. EV5B) and testes (Fig. EV5C), consistent with previous reports (Arama *et al*, 2003, 2007;
254 Kaplan *et al*, 2010; Nezis *et al*, 2010; Hou *et al*, 2008). Western blot analysis revealed Bruce
255 expression in both adult males and females (Fig. EV5D). We also detected Bruce expression in
256 wing imaginal discs (Fig. EV5E). This signal was abolished by the RNAi-mediated knockdown
257 of *Bruce*, confirming the specificity of the signal (Fig. EV5F). These findings indicate that
258 Bruce not only functions in the gonads but can also exert Dcp-1 regulatory functions in wing
259 imaginal discs.
260
261 ***Bruce specifically suppresses Dcp-1 overexpression-induced cell death***
262 Next, we investigated whether Bruce regulated Dcp-1 activity. Upon overexpression of *Bruce*
263 (Fig. 5A), we observed marked suppression of Dcp-1-induced cell death (Fig. 5B, C). Although
264 *DIAP1* overexpression also inhibited Dcp-1 activation, this suppressive effect was stronger
265 following *Bruce* overexpression (Fig. 5B, C). We examined the specificity of Bruce in the

266 regulation of other forms of cell death. As mentioned earlier, the BH3-only protein Synr induces
267 autophagy and Dcp-1-dependent cell death (Ikegawa *et al*, 2023). To investigate whether Bruce
268 was involved in Debcl/Buffy-autophagy-Dcp-1-mediated cell death, we examined the role of
269 Bruce in Synr-induced cell death. Overexpression of *Bruce*, but not *DIAP1*, specifically
270 suppressed Synr-induced cell death (Fig. 5D). In contrast, *Bruce* overexpression failed to rescue
271 the eye ablation phenotype independent of autophagy caused by *Hid* overexpression, whereas
272 DIAP1 fully rescued this phenotype (Fig. 5E). Taken together, these results suggest that Bruce
273 and DIAP1 regulate distinct cell death pathways, with Bruce acting as a selective inhibitor of
274 autophagy-regulated Dcp-1- and Synr-dependent cell death.
275
276 ***Bruce suppresses wing tissue growth***
277 We have previously reported that Dcp-1 activity can promote imaginal tissue growth
278 independent of the core apoptosis signaling pathway, including Dronc (Shinoda *et al*, 2019).
279 To investigate the role of Bruce in imaginal tissue growth, we analyzed its effect on wing
280 imaginal discs using *WP-Gal4*, which drives expression throughout the wing pouch.
281 Overexpression of *p35* suppressed wing tissue growth (Fig. 5F, G), whereas inhibition of
282 canonical apoptotic signaling by $Dronc^{DN}$ and *DIAP1* had no effect (Fig. 5F, G). In contrast,
283 *Bruce* overexpression suppressed wing growth to an extent similar to *p35* overexpression,
284 whereas *Bruce* knockdown tended to increase wing size, although the difference was not
285 statistically significant (Fig. 5F, G). We confirmed these results using *Engrailed-Gal4*, which
286 is expressed in the posterior compartment of the wing imaginal disc. *p35* overexpression
287 suppressed wing tissue growth (Fig. 5H, I). In this context, the inhibition of canonical apoptosis
288 signaling by $Dronc^{DN}$ and *DIAP1* had a minor but negative effect on wing size (Fig. 5H, I).
289 *Bruce* overexpression suppressed wing growth, whereas *Bruce* knockdown increased wing size
290 (Fig. 5H, I), indicating that Bruce negatively regulates wing tissue growth. Finally, to enhance

291 the sensitivity of the assay, we overexpressed the dominant-negative form of the insulin
292 receptor (*InR*^{DN}) using *WP-Gal4*, which significantly reduced wing size (Fig. 5J, K). Under this
293 sensitized condition, simultaneous *Bruce* knockdown significantly enhanced wing tissue
294 growth (Fig. 5J, K). Overall, these results indicate that Bruce suppresses wing tissue growth.
295

296 **Discussion**

297 ***Autophagy-facilitated alternative caspase activation pathway***

298 In this study, we identified a distinct regulatory mechanism governing the activation of the
299 *Drosophila* executioner caspase, Dcp-1, in sharp contrast to its paralog Drice. Although both
300 caspases share structural similarities and are expressed in overlapping tissues, Dcp-1, but not
301 Drice, is activated upon overexpression in an apoptosome-independent, autophagy-regulated
302 manner. Previous studies have implicated Dcp-1 in the induction of autophagy (Hou *et al*, 2008;
303 DeVorkin *et al*, 2014; Choutka *et al*, 2017). Our findings extend this view by showing that
304 autophagy is required for Dcp-1 activation, suggesting a positive feedback loop between Dcp-
305 1 and autophagy during apoptosis. Although the precise downstream targets of the Bcl-2 family
306 proteins, Debcl and Buffy, remain unknown, their roles in autophagy regulation (Hou *et al*,
307 2008) suggest that they influence Dcp-1 activity through autophagic pathways. Additionally,
308 we identified Bruce, a giant inhibitor of apoptotic proteins, as a Dcp-1-specific suppressor.
309 Functionally, Bruce limits wing tissue growth, suggesting that Dcp-1 activation contributes to
310 growth regulation in a non-lethal manner (Shinoda *et al*, 2019). Taken together, our results
311 demonstrate that the regulatory mechanisms of Dcp-1 and Drice diverge at the level of IAPs
312 and that Dcp-1 activation is regulated by autophagy, enabling specific non-lethal functions that
313 promote tissue growth independent of canonical apoptotic signaling (Fig. 5L). It is important
314 to note that Dcp-1 can also suppress autophagy through cleavage of Acinus (Haberman *et al*,
315 2010; Nandi *et al*, 2014). Although this may seem contradictory, the ability of caspases to
316 function in a non-lethal manner requires strict prevention of excessive activation. Such
317 suppression may represent a key mechanism that enables non-lethal caspase activity.

318 It is also important to understand how cells determine the usage of canonical versus
319 alternative caspase activation pathways depending on physiological or environmental
320 conditions. In mammals, two major apoptotic pathways are activated by distinct initiator

321 caspases, caspase-8 and caspase-9, in response to different upstream signals (Newton *et al*,
322 2024). Similarly, in *Drosophila*, while most developmental cell death is driven by canonical
323 apoptotic signaling involving Dronc (Xu *et al*, 2005), alternative caspase activation pathways
324 may be preferentially engaged in response to environmental stimuli, such as starvation or heat
325 shock.
326
327 ***Initiator caspase-independent activation mechanism for Dcp-1***
328 The mechanism by which Dcp-1 is activated by itself remains an open and important question.
329 In contrast to Drice, Dcp-1 is activated upon overexpression in an apoptosome-independent but
330 autophagy-dependent manner. Unlike initiator caspases, executioner caspases such as Dcp-1
331 generally lack long N-terminal prodomains and require proteolytic cleavage to become
332 catalytically active. Proximity-labeling analysis revealed that Dcp-1 was predominantly
333 associated with the chaperonin subunit CCT8 (Fig. 2E). Given that the overexpression of *Dcp-*
334 *1* increases its local concentration for activation, we propose that its accumulation in the
335 chaperonin complex may serve as a local scaffold for caspase activation. This model implies a
336 spatially restricted mode of regulation in which caspase activity is compartmentalized within
337 the cell. In this model, we speculated that Dcp-1 activation occurs sporadically in subcellular
338 regions enriched in activators or scaffolding molecules such as CCT8. Under these conditions,
339 Dcp-1 activation may need to be tightly regulated to prevent its unintended proteolytic activity.
340 Supporting this notion, we proposed that Bruce functions as a basal suppressor of Dcp-1 in non-
341 lethal contexts, restraining caspase activity when full apoptotic signaling is not engaged.
342
343 ***Distinct roles of evolutionarily multiplicated executioner caspases***
344 Caspases are essential cysteine proteases that execute apoptotic cell death and are conserved
345 from *C. elegans* to mammals (Shinoda & Miura, 2024). Multiple executioner caspases exist,

346 including caspase-3 and caspase-7 in mammals and Dcp-1 and Drice in *Drosophila*. Although
347 these enzymes are often functionally redundant in apoptosis, growing evidence indicates that
348 each executioner caspase harbors distinct substrate specificities and fulfills non-overlapping
349 roles (Walsh *et al*, 2008; Boucher *et al*, 2012; Desroches & Denault, 2019; Shinoda *et al*, 2019,
350 2023). In mammals, caspase-3 and caspase-7 exhibit high sequence similarity but differ in their
351 substrate preferences. Caspase-7, for instance, contains polybasic residues in its exosite that
352 enhance its ability to cleave RNA-binding proteins, a function not observed in caspase-3
353 (Boucher *et al*, 2012). Mechanistically, this exosite enables caspase-7 to interact directly with
354 RNA, thereby promoting selective proteolysis of RNA-associated substrates (Desroches &
355 Denault, 2019). Furthermore, we have recently demonstrated that caspase-7 is essential for
356 early-peaking caspase activity at the plasma membrane during apoptosis, a process mediated
357 by its N-terminal intrinsically disordered region, which facilitates rapid efferocytosis of
358 apoptotic cells (Taira *et al*, 2025). In this study, we demonstrated that *Drosophila* executioner
359 caspases Dcp-1 and Drice are also subject to distinct activation mechanisms for the specific
360 non-lethal function of tissue growth. These findings underscore that the evolutionary expansion
361 of executioner caspases does not merely provide functional redundancy for apoptotic execution
362 but rather confers unique biochemical properties and regulatory roles under distinct cellular
363 contexts. This diversification allows executioner caspases to participate in both lethal and non-
364 lethal cellular processes, highlighting their broader functional repertoire beyond canonical
365 apoptosis.
366

367 **Methods**

368 ***Fly strains and rearing conditions***

369 We raised the flies in standard *Drosophila* medium at 25°C. For in vivo biotin labeling
370 experiments, flies were raised in standard *Drosophila* medium supplemented with 100 μM (+)-
371 biotin (#029-08713, WAKO). The fly strains used in this study are listed in Table EV2.
372 Genotypes corresponding to each figure are shown in Table EV3.

373

374 ***Intrinsically disordered region prediction***

375 Amino acid sequences were obtained from the FlyBase database [https://flybase.org/].
376 Disordered regions were predicted using the PSIPRED protein sequence analysis workbench in
377 DISOPRED3 [http://bioinf.cs.ucl.ac.uk/psipred/].

378

379 ***Adult wings and eyes phenotypes scoring***

380 Adult female flies were anesthetized using CO_2. The wing and eye images were acquired using
381 a Leica MZ16F fluorescent stereomicroscope (Leica Microsystems) equipped with a Leica
382 DFC450 C CCD camera. Each wing was manually classified into one of four categories: *Intact*
383 (no defect), *Mild* (≧50% of wing area intact), *Severe* (<50% but ≧5% of wing area intact), and
384 *Wingless* (<5% of wing area intact).

385

386 ***Molecular cloning***

387 For *pAc5-Caspases-myc-mNeonGreen*, the coding sequences of *Dcp-1* and *Drice* were
388 amplified using PCR from the corresponding *pUASz-Caspase::V5::TurboID* plasmids
389 (Muramoto *et al*, 2025). The coding sequence of myc-tagged mNeonGreen was PCR-amplified
390 from *pUASz-Drice::myc::mNeonGreen plasmid* (Muramoto *et al*, 2025). The two fragments

391 were ligated into EcoRI/XhoI-digested *pAc5_STABLE2_neo* (González *et al*, 2011) using In-
392 Fusion (TaKaRa, Z9648N).

393 For *pCold I-EcoRI-CCT8-EcoRI*, the coding sequence of *CCT8* was PCR-amplified
394 from *Drosophila* cDNA, and the fragment was ligated into the *Eco*RI-digested *pCold I DNA*
395 vector (#3361, TaKaRa) using In-Fusion.

396 For *pAc5-Caspases^{CG}-myc*, the coding sequences of *Dcp-1* and *Drice* were PCR
397 amplified from the corresponding *pAc5-Caspases-myc-mNeonGreen* plasmids. The fragments
398 were ligated into EcoRI/BamHI-digested *pAc5_STABLE2_neo* (González *et al*, 2011) using In-
399 Fusion. For pAct-Bruce$^{1\text{-}900a}$a-3xFLAG, the first 900 aa of the coding sequences of *Bruce* were
400 PCR-amplified from *Drosophila* cDNA, and the fragment was ligated into the *Eco*RI-digested
401 *pAc5-Fasciclin 3 isoform A-3xFLAG* plasmids (Muramoto *et al*, 2025) using In-Fusion. For
402 *pAc5-3xFLAG-mRuby*3, *Drosophila* codon-optimized mRuby3 was synthesized (Integrated
403 DNA Technologies, Coralville, IA, USA) and ligated into the BamHI-digested *pAc5-3xFLAG-*
404 *Bub3* plasmids (Shinoda *et al*, 2023) using In-Fusion.

405 For mStayGold::C4 linker::V5-tag knock-in for Bruce, the guide RNA was identified
406 using the CRISPR Optimal Target Finder tool available on flyCRISPR
407 [http://flycrispr.molbio.wisc.edu/]. The DNA fragments for the guide RNA were subcloned into
408 BbsI-digested pDCC6 vectors (#59985, Addgene) (Gokcezade *et al*, 2014) to establish the
409 *pDCC6-dBruce-sgRNA* plasmid. The following primers were annealed to generate the DNA
410 fragments for guide RNAs: 5′-CTTCGCTTGCTTGAGGACGCGCTGC-3′ and 5′-
411 AAACGCAGCGCGTCCTCAAGCAAGC-3′. For the generation of the homology-directed
412 repair template (*pBac-mStayGold-c4-V5-dBruce-donor-3xP3-dsRed-polyA*), DNA fragments
413 of the 5′ homology arm were assembled into the BsaI site, and the DNA fragment of the 3′
414 homology arm with mStayGold::C4 linker::V5-tag was assembled into the SapI site of
415 pBac[3xP3-DsRed_polyA_Scarless_TK] (Shinoda *et al*, 2019) using In-Fusion. The PAM

416 sequence (TGG) of the gRNA-binding sites in the donor template was mutated (TGA) to
417 prevent Cas9-directed cleavage following homology-directed repair. The mStayGold::C4
418 linker::V5-tag fragment was amplified from pRSETB/mStayGold(c4) (#212018; Addgene)
419 (Ando *et al*, 2024) with V5-tag harboring primers. DNA fragments were amplified using PCR
420 with the following primers: dBruce 5′ homology arm (forward primer, 5′-
421 TGAAGGTCTCCTTAAAAGCCCGATTGGCGGCGCAGGAAGT-3′, and reverse primer,
422 5′-TCTTTCTAGGGTTAATCGAGTGCCCAGGGGGCGCGCGAGT-3′), dBruce 3′
423 homology arm-1 (forward primer, 5′-
424 TCTTTCTAGGGTTAATTTTTGGCATTCACAGGCGATTGCT-3′, and reverse primer, 5′-
425 TCCGGAGGTGCGCCGCGGCAATTTG-3′), mStayGold-C4 linker-V5-tag (forward primer,
426 5′-CGGCGCACCTCCGGAATGGTGTCTACAGGCGAGGAGCTGT-3′, and reverse primer,
427 5′-
428 GGTGCTGTCCAGGCCCAGCAGGGGGTTGGGGATGGGCTTGCCCACGGCAGAAGC
429 AGAAGGCTCGTGC-3′), 3′ homology arm-2 with mutated PAM (forward primer, 5′-
430 GGCCTGGACAGCACCGCCACGGAGCAGCATCATCAGCAGCGCGTCCTCAA-3′, and
431 reverse primer, 5′-GACGGCTCTTCATTAACTCTTAAATCAAATTTAAATTGAA-3′). The
432 established plasmids were injected into *yw; nos-Cas9(II-attP40)* for CRISPR/Cas9-mediated
433 transgenesis (BestGene Inc.). Each DsRed-positive transformant was isogenized and confirmed
434 using genomic PCR and sequencing.
435 All established plasmids were sequenced by Eurofins, Inc. The detailed plasmid DNA
436 sequences are available upon request.
437
438 ***Cell culture***

439 *Drosophila* S2 cells were grown at 25°C in Schneider's *Drosophila* medium (GIBCO,
440 21720001) supplemented with 10% (v/v) heat-inactivated fetal bovine serum, 100 U/mL
441 penicillin, and 100 μg/mL streptomycin (WAKO, 168-23191).
442
443 ***mNeonGreen signal quantification of S2 cells***
444 *Drosophila* S2 cells (2.5×10^5) seeded in 24-well plates were transfected with 200 ng of the
445 desired plasmid using Effectene Transfection Reagent (QIAGEN, 301427) following the
446 manufacturer's protocol. Sixteen hours after transfection, cells were transferred to four-
447 compartment glass-bottomed dishes (Greiner #627870). After another 24 hours, images were
448 captured using a Leica TCS SP8 confocal microscope (Leica Microsystems).
449 The mNeon Green intensity was quantified using Fiji (ImageJ) software (NIH Image).
450 Images were analyzed automatically using the ImageJ macro, as previously described (Fujisawa
451 *et al*, 2020) with modifications. Briefly, the mNeonGreen channel was filtered by the "Gaussian
452 Blur (sigma = 1)", processed with "Auto Threshold ("Mean" method)," processed with
453 "Watershed," and processed with "Analyze particles (size = 40–200 μm^2, circularity = 0.2–1.0)"
454 to define the region of interest. For a given region of interest, the average mNeon Green
455 intensity was measured.
456
457 ***Protein preparation of Drosophila tissues***
458 Whole larvae without digestive tract and fatobodies, larval salivary glands, fatbodies, brains,
459 wing discs and whole adults, adult thoraxes, ovaries, and testises of desired genotype were
460 dissected and lysed with RIPAi buffer (50 mM Tris-HCl, pH 8.0, 150 mM sodium chloride, 0.5
461 wt/vol% sodium deoxycholate, 0.1% w/v sodium dodecyl sulfate, and 1.0% w/v NP-40)
462 supplemented with cOmplete ULTRA EDTA-free protease inhibitor cocktail (#05892953001,
463 Roche). Samples were homogenized and centrifuged at 20,000 × *g*, 4°C for 10 min. The

464 supernatants were collected and snap-frozen in liquid nitrogen. Protein concentrations were
465 determined using the BCA assay (#297-73101, Wako) following the manufacturer's protocol.
466 The samples were mixed with Laemmli buffer, boiled at 95°C for 5 min, and then subjected to
467 western blotting analysis.
468
469 ***Western blotting***
470 Each sample was separated using SDS-PAGE. The proteins were then transferred onto
471 Immobilon-P polyvinylidene fluoride membranes (#IPVH00010; Millipore) for
472 immunoblotting. Membranes were blocked with 4% skim milk diluted in 1× TBST.
473 Immunoblotting was performed using the antibodies mentioned below, which were diluted with
474 4% skim milk. Signals were visualized using Immobilon Western Chemiluminescent HRP
475 Substrate (#WBKLS0500; Millipore) and FUSION SOLO. 7S. EDGE (Vilber-Lourmat).
476 Contrast and brightness adjustments were applied equally using Fiji (ImageJ) software (NIH
477 Image).
478 The primary antibodies used included mouse anti-V5 monoclonal antibody (1:1,000,
479 #46-0705, Invitrogen), mouse anti-FLAG M2 monoclonal antibody (1:5,000, Sigma), rabbit
480 anti-CCT8 polyclonal antibody (1:5,000, this study), rabbit anti-Myc-Tag (71D10) monoclonal
481 antibody (1:5,000, #2278, CST), rabbit anti-3xDYKDDDDK Tag (3xFLAG Tag) (E7C5T)
482 monoclonal antibody (1:5,000, #87537, CST), mouse anti-alpha tubulin (DM1A) monoclonal
483 antibody (1:10,000, #T9026, Sigma), mouse anti-Histone H3 (1B1B2) monoclonal antibody
484 (1:10,000, #14269, CST), and mouse anti-Actin monoclonal antibody (1:5,000; #A4700,
485 Sigma). The secondary antibodies used were goat anti-rabbit IgG horseradish peroxidase
486 (HRP)-conjugated antibody (1:5,000, #7074S, CST) and goat/rabbit/donkey anti-mouse IgG
487 HRP Conjugate (1:5,000, #W402B, Promega). The membranes for streptavidin blotting were

488 blocked with 3% bovine serum albumin. Streptavidin blotting was performed using
489 streptavidin-HRP (1:10,000, #SA10001; Invitrogen) diluted in 3% bovine serum albumin.
490
491 ***Experimental design for liquid chromatography–mass spectrometry (LC-MS/MS) analyses***
492 Two biological replicates were analyzed for each experimental condition to determine the
493 abundance of Drice/Dcp-1::TurboID relative to the control.
494
495 ***Purification of biotinylated proteins***
496 Samples were prepared as previously described (Shinoda *et al*, 2023). Briefly, 100 μg of
497 biotinylated protein-containing lysate was subjected to FG-NeutrAvidin bead (#TAS8848
498 N1171, Tamagawa Seiki) purification. FG-NeutrAvidin beads (25 μL, approximately 500 μg)
499 were washed three times with RIPA buffer. Benzonase-treated biotinylated protein samples
500 suspended in 1 mL of RIPA buffer were incubated overnight at 4°C. Conjugated beads were
501 magnetically isolated and washed with 500 μL of an ice-cold RIPA buffer solution, 1 M KCl
502 solution, 0.1 M Na_2CO_3 solution, and 4 M urea solution. For western blot analyses, the purified
503 samples were mixed with Laemmli buffer, boiled at 95°C for 5 min, and then subjected to
504 western blot analysis. For LC-MS/MS analysis, the purified samples were washed with 500 μL
505 ultrapure water (#214-01301, Wako) and 500 μL of 50 mM ammonium bicarbonate. The
506 samples were then mixed with 50 μL of 0.1% Rapigest diluted in 50 mM ammonium
507 bicarbonate, and 5 μL of 50 mM TCEP was subsequently added. Samples were incubated at
508 60°C for 5 min, and then 2.5 μL of 200 mM methyl methanethiosulfonate was added. One
509 microgram sequence-grade modified trypsin (#V5111, Promega) was then added for on-bead
510 trypsin digestion at 37°C, leaving the treatment for 16 h. The beads were then magnetically
511 isolated, and 60 μL of the supernatant was collected. Then, 3 μL of 10% trifluoroacetic acid
512 was added to the supernatants, incubating them at 37°C for 60 min with gentle agitation. The

513 samples were then centrifuged at 20,000 × *g*, 4°C for 10 min. The peptides were then
514 desalinated and purified using a GL-tip SDB (#7820-11200, GL Sciences) following the
515 manufacturer's instructions. The samples were speed-backed at 45°C for 30 min and dissolved
516 in 25 µL of 0.1% formic acid. The samples were then centrifuged at 20,000 × *g*, 4°C for 10
517 min, and the supernatants were collected. The peptide concentrations were determined using
518 the BCA assay. Finally, 500 ng of the purified protein was subjected to LC-MS/MS analysis.
519
520 ***LC-MS/MS analyses***
521 Samples were loaded onto an Acclaim PepMap 100 C18 column (75 µm x 2 cm, 3 µm particle
522 size and 100 Å pore size; #164946, Thermo Fisher Scientific) and separated on a nano-capillary
523 C18 column, (75 µm x 12.5 cm, 3 µm particle size, #NTCC-360/75-3-125, Nikkyo Technos)
524 using EASY-nLC 1200 system (Thermo Fisher Scientific). Elution conditions are listed in
525 Table EV4. The separated peptides were analyzed using QExactive (Thermo Fisher Scientific)
526 in data-dependent MS/MS mode. The parameters for the MS/MS analysis are listed in Table
527 EV5. The collected data were analyzed using Proteome Discoverer (PD) 2.2 software with the
528 Sequest HT search engine. The parameters for the PD 2.2 analysis are described in Table EV6.
529 Peptides were filtered at a false discovery rate of 0.01 using the Percolator node. Label-free
530 quantification was performed based on the intensities of the precursor ions using a precursor-
531 ion quantifier node. Normalization was performed using the total amount of peptides in all
532 average scaling modes. MS proteomic data were deposited in the ProteomeXchange
533 Consortium via the jPOST partner repository with the dataset identifier PXD067425 (Okuda *et*
534 *al*, 2017).
535
536 ***Anti-CCT8 antibody generation***

537 CCT8 was expressed in *Escherichia coli BL21* transformed with *pCold I-EcoRI-CCT8-EcoRI*.
538 Cells were grown at 37 °C overnight, diluted to OD_{600} 0.2 and cultured until OD_{600} 0.5 at 37°C.
539 Protein expression was induced by the addition of 1 mM IPTG at 15°C for 24 h. Cells were
540 centrifuged at 4000 × *g*, 4 °C for 20 min and resuspended in phosphate-buffered saline (PBS).
541 Cells were centrifuged at 4000 × *g*, 4°C for 10 min. Purification of 6x His-tagged CCT8 was
542 performed using the QIAexpress Ni-NTA Fast Start Kit (#30600, Qiagen) according to the
543 manufacturer's protocol: purification of 6xHis-tagged proteins under denaturing conditions.
544 Briefly, the cell pellets were lysed in Lysis Buffer (Denaturing Buffer adjusted to pH 8.0) with
545 gentle agitation for 60 min. The sample was centrifuged at 9,200 × *g*, 20°C for 30 min. The
546 supernatant was applied to Fast Start column and washed twice with Wash Buffer (Denaturing
547 Buffer adjusted to pH 6.3). Proteins were eluted using Elution Buffer (Denaturing Buffer
548 adjusted to pH 4.5). Polyclonal antibodies were raised in rabbits using purified 6xHis-tagged
549 CCT8 as an immunogen (Eurofins Inc.).
550
551 ***Protein complexes prediction with AlphaFold3***
552 Amino acid sequences were obtained from the FlyBase database [https://flybase.org/]. The
553 protein complex structures were predicted using AlphaFold3 (Abramson *et al*, 2024) on the
554 AlphaFold server [https://alphafoldserver.com/].
555
556 ***Co-immunoprecipitation***
557 *Drosophila* S2 cells (2.0×10^6) seeded in 6-well plates were transfected with the desired
558 plasmid using Effectene Transfection Reagent. For live cell lysate, *Drosophila* S2 cells were
559 lysed on ice using 550 µL of IP lysis buffer (50 mM Tris-HCl (pH 7.5), 150 mM NaCl, 0.5%
560 NP-40) supplemented with cOmplete ULTRA EDTA-free protease inhibitor cocktail. For
561 apoptotic cell lysate, the cells were treated with 10 µg/mL cycloheximide (#C7698, Sigma) for

562 apoptosis induction. After 6 h of incubation, cells were harvested and centrifuged at 800 × *g*,
563 4 °C for 5 min and washed twice. Then, cells were lysed by using 550 μL of IP lysis buffer (50
564 mM Tris-HCl (pH 7.5), 150 mM NaCl, and 0.5% NP-40) supplemented with cOmplete
565 ULTRA EDTA-free protease inhibitor cocktail. The cell lysates were centrifuged at 20,000 × *g*,
566 4 °C for 5 min. Supernatants (50 μL) were collected as inputs. The remainder of the supernatant
567 was incubated for 2 h at 4°C with 20 μL of anti-DDDDK-tag mAb-Magnetic Agarose (#M185-
568 10R, MBL) equilibrated with the IP lysis buffer. The beads were washed thrice in IP lysis buffer
569 and boiled for 5 min at 95°C with 50 μL 1× Laemmli buffer. The samples were magnetically
570 separated, and the supernatants were subjected to SDS-PAGE.
571
572 ***Immunohistochemistry***
573 Wing imaginal discs of the late third-instar larvae and testes and ovaries of the adults were fixed
574 with 4% paraformaldehyde in PBS. The wing imaginal discs and testes samples were washed
575 in PBS containing 0.1% Triton X-100 (PBST), and the ovary samples were washed in 1.0%
576 PBST, blocked in PBST with 5% normal donkey serum (PBSTn) for 30 min, and incubated
577 with primary antibodies in PBSTn overnight at 4°C. The samples were washed with PBST,
578 incubated for 2 h with secondary antibodies suspended in PBSTn, and washed again with PBST.
579 Images were captured using a TCS SP8 microscope (Leica Microsystems).
580 The primary antibodies used were mouse anti-Myc-tag monoclonal antibody (1:500,
581 #R950-25, Invitrogen) and mouse anti-V5 tag monoclonal antibody (1:100, #960-25,
582 Invitrogen). The secondary antibodies used were Alexa488-conjugated donkey anti-mouse IgG
583 (1:500 (Myc) or 1:100 (V5), #A-21202, Thermo Fisher Scientific). Hoechst 33342 (8 μM;
584 #H3570, Invitrogen) for nuclear staining was used during the secondary antibody incubation.
585 Images were analyzed and edited using ImageJ software.
586

587 ***Wing size measurement***

588 Flies were raised, and their wings were mounted and digitized as previously described (Shinoda
589 *et al*, 2019). Briefly, flies were placed on an acetic acid agar plate (2% agar, 1% sucrose, and
590 0.36% acetic acid) to lay eggs overnight. The plates were collected, and the eggs were incubated
591 at 25°C for 24 h. The 1st instar larvae were collected from the agar plate, and 30 larvae were
592 placed in one vial to precisely control the larval density. These flies were raised at 25°C. After
593 more than two days of hatching, the adult female flies were collected and submerged in 99.5%
594 ethanol to dehydrate for 24 hours. Dehydrated flies were dissected to mount their wings using
595 Euparal (Waldeck) with the dorsal side upward. Images were digitized using an upright
596 microscope (Leica DM5000B; Leica Microsystems) equipped with a CCD camera. The wing
597 size was measured using a Drosophila wing digital twin
598 [https://datamarkin.com/models/drosophila-wings-beta] developed by Datamarkin. Areas 0, 1,
599 and 2 were quantified as the anterior parts, whereas areas 4, 6, 7, and 8 were quantified as the
600 posterior parts, respectively.

601

602 ***Statistical analysis***

603 The data are presented as the means ± standard error of measurement (SEM). *p*-values were
604 calculated using a one-way analysis of variance (ANOVA), followed by Sidak's multiple
605 comparison test for selected pairs (Fig. EV1B, C, D; Fig. 5K), or Dunnett's multiple comparison
606 test using GraphPad Prism 8. NS: $p \geqq 0.05$, †: $p < 0.05$.

607

608 **Acknowledgments**

609 We would like to thank G. W. Davis, R. Carthew, B. Hay, C-H. Cheng, H. Richardson, S. K.
610 Yoo, H. Steller, Y. Hiromi, H. D. Ryoo, the FlyORF Zurich ORFeome Project, Bloomington
611 *Drosophila* Stock Center, Vienna Drosophila Resource Center, Kyoto Stock Center, and NIG-
612 FLY for providing the fly strains. We thank Datamarkin for providing the Drosophila wing
613 digital twin tool. We thank Dr. S. Hirayama, Dr. S. Murata, and the One-Stop Sharing Faculty
614 Center for Future Drug Discovery at the Graduate School of Pharmaceutical Sciences,
615 University of Tokyo, for the LC-MS/MS analysis. We thank Miura's lab members for their
616 technical assistance and discussions; in particular, K. Takenaga for preparing the fly food and
617 R. Takamoto for experimental support. We thank *Editage* [www.editage.com] for the English
618 language editing of this manuscript. This work was supported by grants from the Ministry of
619 Education, Culture, Sports, Science, and Technology of Japan (KAKENHI Grant Numbers
620 19K16137, 21K15080, 22H05586, and 23K05747 to N.S. and 21H04774, 23H04766,
621 24H00567, and 25H01842 to M.M.), the Japan Agency for Medical Research and Development
622 (AMED; Grant number JP21gm5010001 to M.M.), and grants from the Takeda Science
623 Foundation and Sumitomo Foundation to N.S.

624

625 **Author Contributions**

626 N.S. and M.M. designed the study; N.S. conducted most of the experiments and analyzed most
627 of the data; Y.H conducted protein structural predictions; N.H. analyzed the expression patterns
628 of Drosophila caspases; and N.S. and M.M. wrote the manuscript.

629

630 **Conflict of Interest**

631 The authors declare that they have no conflict of interest.

632

633 **References**

634 Abramson J, Adler J, Dunger J, Evans R, Green T, Pritzel A, Ronneberger O, Willmore L,
635 Ballard AJ, Bambrick J, *et al* (2024) Accurate structure prediction of biomolecular
636 interactions with AlphaFold 3. *Nature* 630: 493–500

637 Ando R, Shimozono S, Ago H, Takagi M, Sugiyama M, Kurokawa H, Hirano M, Niino Y,
638 Ueno G, Ishidate F, *et al* (2024) StayGold variants for molecular fusion and membrane-
639 targeting applications. *Nat Methods* 21: 648–656

640 Aram L, Yacobi-Sharon K & Arama E (2017) CDPs: caspase-dependent non-lethal cellular
641 processes. *Cell Death Differ* 24: 1307–1310

642 Arama E, Agapite J & Steller H (2003) Caspase activity and a specific cytochrome C are
643 required for sperm differentiation in Drosophila. *Dev Cell* 4: 687–697

644 Arama E, Bader M, Rieckhof GE & Steller H (2007) A ubiquitin ligase complex regulates
645 caspase activation during sperm differentiation in Drosophila. *PLoS Biol* 5: e251

646 Berthelet J & Dubrez L (2013) Regulation of apoptosis by inhibitors of apoptosis (IAPs). *Cells*
647 2: 163–187

648 Boucher D, Blais V & Denault J-B (2012) Caspase-7 uses an exosite to promote poly(ADP
649 ribose) polymerase 1 proteolysis. *Proc Natl Acad Sci U S A* 109: 5669–5674

650 Branon TC, Bosch JA, Sanchez AD, Udeshi ND, Svinkina T, Carr SA, Feldman JL, Perrimon
651 N & Ting AY (2018) Efficient proximity labeling in living cells and organisms with
652 TurboID. *Nat Biotechnol* 36: 880–887

653 Choutka C, DeVorkin L, Go NE, Hou Y-CC, Moradian A, Morin GB & Gorski SM (2017)
654 Hsp83 loss suppresses proteasomal activity resulting in an upregulation of caspase-
655 dependent compensatory autophagy. *Autophagy* 13: 1573–1589

656 Desroches A & Denault J-B (2019) Caspase-7 uses RNA to enhance proteolysis of poly(ADP-
657 ribose) polymerase 1 and other RNA-binding proteins. *Proc Natl Acad Sci U S A* 116:
658 21521–21528

659 DeVorkin L, Go NE, Hou Y-CC, Moradian A, Morin GB & Gorski SM (2014) The Drosophila
660 effector caspase Dcp-1 regulates mitochondrial dynamics and autophagic flux via SesB.
661 *J Cell Biol* 205: 477–492

662 Ditzel M, Broemer M, Tenev T, Bolduc C, Lee TV, Rigbolt KTG, Elliott R, Zvelebil M,
663 Blagoev B, Bergmann A, *et al* (2008) Inactivation of effector caspases through
664 nondegradative polyubiquitylation. *Mol Cell* 32: 540–553

665 Domingues C & Ryoo HD (2012) Drosophila BRUCE inhibits apoptosis through non-lysine
666 ubiquitination of the IAP-antagonist REAPER. *Cell Death Differ* 19: 470–477

667 Ehrmann JF, Grabarczyk DB, Heinke M, Deszcz L, Kurzbauer R, Hudecz O, Shulkina A,
668 Gogova R, Meinhart A, Versteeg GA, *et al* (2023) Structural basis for regulation of
669 apoptosis and autophagy by the BIRC6/SMAC complex. *Science* 379: 1117–1123

670 Florentin A & Arama E (2012) Caspase levels and execution efficiencies determine the
671 apoptotic potential of the cell. *J Cell Biol* 196: 513–527

672 Fujisawa Y, Shinoda N, Chihara T & Miura M (2020) ROS Regulate Caspase-Dependent Cell
673 Delamination without Apoptosis in the Drosophila Pupal Notum. *iScience* 23: 101413

674 Furuyama T, Banerjee R, Breen TR & Harte PJ (2004) SIR2 is required for polycomb silencing
675 and is associated with an E(Z) histone methyltransferase complex. *Curr Biol* 14: 1812–
676 1821

677 Gokcezade J, Sienski G & Duchek P (2014) Efficient CRISPR/Cas9 plasmids for rapid and
678 versatile genome editing in Drosophila. *G3 (Bethesda)* 4: 2279–2282

679 González M, Martín-Ruíz I, Jiménez S, Pirone L, Barrio R & Sutherland JD (2011) Generation
680 of stable Drosophila cell lines using multicistronic vectors. *Sci Rep* 1: 75

681 Haberman AS, Akbar MA, Ray S & Krämer H (2010) Drosophila acinus encodes a novel
682 regulator of endocytic and autophagic trafficking. *Development* 137: 2157–2166

683 Hou Y-CC, Chittaranjan S, Barbosa SG, McCall K & Gorski SM (2008) Effector caspase Dcp-
684 1 and IAP protein Bruce regulate starvation-induced autophagy during Drosophila
685 melanogaster oogenesis. *J Cell Biol* 182: 1127–1139

686 Hunkeler M, Jin CY & Fischer ES (2023) Structures of BIRC6-client complexes provide a
687 mechanism of SMAC-mediated release of caspases. *Science* 379: 1105–1111

688 Ikegawa Y, Combet C, Groussin M, Navratil V, Safar-Remali S, Shiota T, Aouacheria A &
689 Yoo SK (2023) Evidence for existence of an apoptosis-inducing BH3-only protein,
690 sayonara, in Drosophila. *EMBO J* 42: e110454

691 Jacomin A-C, Petridi S, Di Monaco M, Bhujabal Z, Jain A, Mulakkal NC, Palara A, Powell EL,
692 Chung B, Zampronio C, *et al* (2020) Regulation of Expression of Autophagy Genes by
693 Atg8a-Interacting Partners Sequoia, YL-1, and Sir2 in Drosophila. *Cell Rep* 31: 107695

694 Julien O & Wells JA (2017) Caspases and their substrates. *Cell Death Differ* 24: 1380–1389

695 Kaplan Y, Gibbs-Bar L, Kalifa Y, Feinstein-Rotkopf Y & Arama E (2010) Gradients of a
696 ubiquitin E3 ligase inhibitor and a caspase inhibitor determine differentiation or death
697 in spermatids. *Dev Cell* 19: 160–173

698 Kim Y-I, Ryu T, Lee J, Heo Y-S, Ahnn J, Lee S-J & Yoo O (2010) A genetic screen for
699 modifiers of Drosophila caspase Dcp-1 reveals caspase involvement in autophagy and
700 novel caspase-related genes. *BMC Cell Biol* 11: 9

701 Liu S-S, Jiang T-X, Bu F, Zhao J-L, Wang G-F, Yang G-H, Kong J-Y, Qie Y-F, Wen P, Fan
702 L-B, *et al* (2024) Molecular mechanisms underlying the BIRC6-mediated regulation of
703 apoptosis and autophagy. *Nat Commun* 15: 891

704 Muramoto M, Hanawa N, Okumura M, Chihara T, Miura M & Shinoda N (2025) Executioner
705 caspase is proximal to Fasciclin 3 which facilitates non-lethal activation in Drosophila
706 olfactory receptor neurons. *Elife* 13

707 Nakajima Y-I & Kuranaga E (2017) Caspase-dependent non-apoptotic processes in
708 development. *Cell Death Differ* 24: 1422–1430

709 Nandi N, Tyra LK, Stenesen D & Krämer H (2014) Acinus integrates AKT1 and subapoptotic
710 caspase activities to regulate basal autophagy. *J Cell Biol* 207: 253–268

711 Newman BL, Lundblad JR, Chen Y & Smolik SM (2002) A Drosophila homologue of Sir2
712 modifies position-effect variegation but does not affect life span. *Genetics* 162: 1675–
713 1685

714 Newton K, Strasser A, Kayagaki N & Dixit VM (2024) Cell death. *Cell* 187: 235–256

715 Nezis IP, Shravage BV, Sagona AP, Lamark T, Bjørkøy G, Johansen T, Rusten TE, Brech A,
716 Baehrecke EH & Stenmark H (2010) Autophagic degradation of dBruce controls DNA
717 fragmentation in nurse cells during late Drosophila melanogaster oogenesis. *J Cell Biol*
718 190: 523–531

719 Okuda S, Watanabe Y, Moriya Y, Kawano S, Yamamoto T, Matsumoto M, Takami T,
720 Kobayashi D, Araki N, Yoshizawa AC, *et al* (2017) jPOSTrepo: an international
721 standard data repository for proteomes. *Nucleic Acids Res* 45: D1107–D1111

722 Qin W, Cho KF, Cavanagh PE & Ting AY (2021) Deciphering molecular interactions by
723 proximity labeling. *Nat Methods* 18: 133–143

724 Shinoda N, Hanawa N, Chihara T, Koto A & Miura M (2019) Dronc-independent basal
725 executioner caspase activity sustains Drosophila imaginal tissue growth. *Proc Natl*
726 *Acad Sci U S A* 116: 20539–20544

727 Shinoda N, Horikoshi M, Taira Y, Muramoto M, Hirayama S, Murata S & Miura M (2023)
728 Caspase cleaves Drosophila BubR1 to modulate spindle assembly checkpoint function
729 and lifespan of the organism. *FEBS J* 290: 4200–4223

730 Shinoda N & Miura M (2024) Exploring caspase-dependent non-lethal cellular processes using
731 Drosophila. *Front Cell Death* 3: 1472108

732 Taira Y, Yang Z, Miyata Y, Shirasaki Y, Segawa K, Miura M & Shinoda N (2025) Early-
733 peaking caspase-7 activity at the plasma membrane drives apoptotic phosphatidylserine
734 exposure. *bioRxiv*: 2025.03.17.643603

735 Tyra LK, Nandi N, Tracy C & Krämer H (2020) Yorkie growth-promoting activity is limited
736 by Atg1-mediated phosphorylation. *Dev Cell* 52: 605-616.e7

737 Vaux DL & Silke J (2005) IAPs, RINGs and ubiquitylation. *Nat Rev Mol Cell Biol* 6: 287–297

738 Walsh JG, Cullen SP, Sheridan C, Lüthi AU, Gerner C & Martin SJ (2008) Executioner
739 caspase-3 and caspase-7 are functionally distinct proteases. *Proc Natl Acad Sci U S A*
740 105: 12815–12819

741 Wu G, Chai J, Suber TL, Wu JW, Du C, Wang X & Shi Y (2000) Structural basis of IAP
742 recognition by Smac/DIABLO. *Nature* 408: 1008–1012

743 Xie HB & Golic KG (2004) Gene deletions by ends-in targeting in Drosophila melanogaster.
744 *Genetics* 168: 1477–1489

745 Xu D, Li Y, Arcaro M, Lackey M & Bergmann A (2005) The CARD-carrying caspase Dronc
746 is essential for most, but not all,developmental cell death in*Drosophila*. *Development*
747 132: 2125–2134

748

749 **Figures and figure legends**

750 **Figure 1**

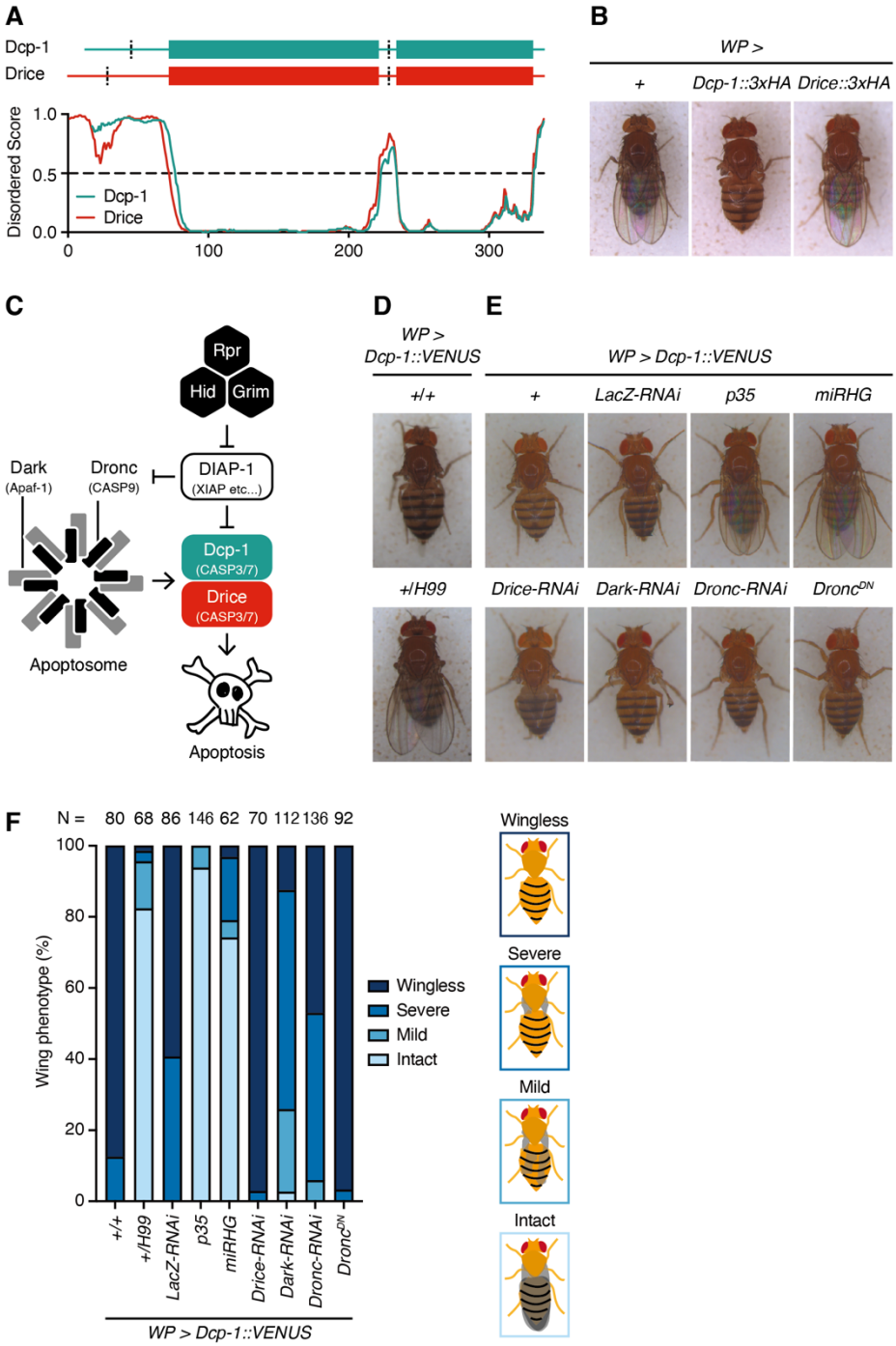

751
752

753 **Figure 1. *Dcp-1* overexpression induces apoptosis independent of the apoptosome.**
754 (A) Schematic structures and intrinsically disordered region prediction of Dcp-1 (dark cyan)
755 and Drice (red). The predicted disordered score plot is shown. Regions wherein the score is
756 more than 0.5 are predicted to be disordered.
757 (B) Representative images of female wing phenotypes upon caspase overexpression using *WP-*
758 *Gal4*.
759 (C) Schematic diagram of canonical apoptosis signaling in *Drosophila*.

760 (D, E) Representative images of female wing phenotypes upon *Dcp-1::VENUS* overexpression
761 using *WP-Gal4* with the genetic perturbation of canonical apoptosis signaling.
762 (F) Quantification of (D) and (E). Each wing is manually classified into four (wingless, severe,
763 mild, and intact) categories. Schematic images of the four categories are shown on the right.
764 Sample sizes are shown in the figure.
765

766 **Figure EV1**

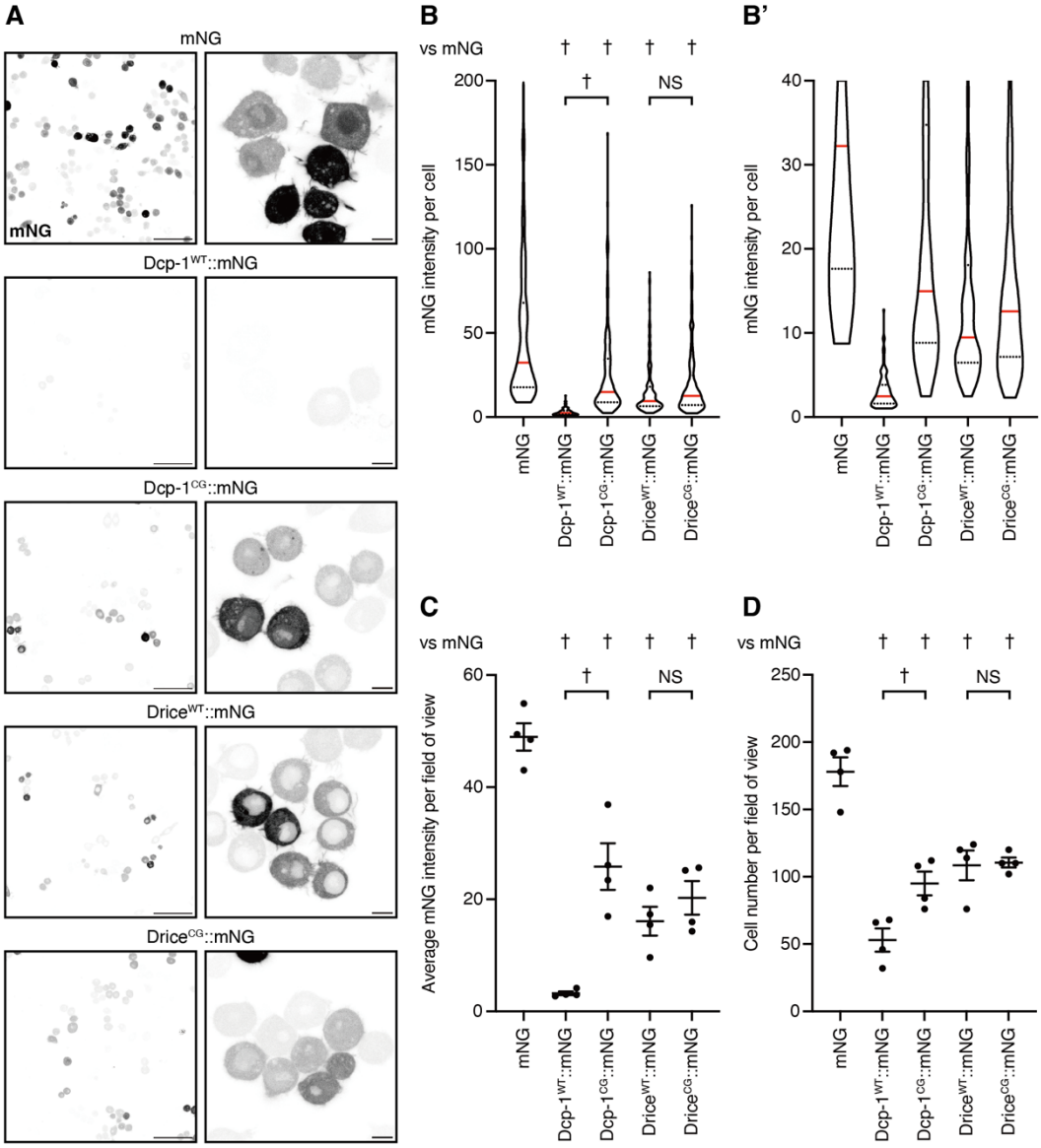

767

768

769 **Figure EV1. Dcp-1 overexpression induces apoptosis in *Drosophila* S2 cells.**
770 (A) Representative images of *Drosophila* S2 cells transfected with mNeonGreen (mNG)-tagged
771 wild-type (WT) or catalytically inactive (catalytic cysteine mutated to glycine; CG) Dcp-1 and
772 Drice. Scale bars: 50 µm (left) and 5 µm (right).
773 (B) Quantification of mNG intensity for each cell, shown as a violin plot. Quartiles are indicated
774 by black broken lines, and the median is indicated by a red bar. (B′) Magnified view of the data
775 in (B), with the Y-axis limited to 0–40. *p*-values were calculated using one-way analysis of
776 variance (ANOVA) followed by Sidak's multiple-comparison test for selected pairs. NS, $p >$
777 0.05; †, $p < 0.05$. Sample sizes: mNG (n = 712 cells), Dcp-1^{WT}::mNG (n = 212 cells), Dcp-
778 1^{CG}::mNG (n = 380 cells), $Drice^{WT}$::mNG (n = 434 cells), and $Drice^{CG}$::mNG (n = 442 cells).
779 (C) Quantification of the average mNG intensity in each field of view. Data are presented as
780 mean ± SEM. *p*-values were calculated using one-way ANOVA followed by Sidak's multiple-

781 comparison test for selected pairs. NS, $p \geqq 0.05$; †, $p < 0.05$. Sample size for each condition is
782 4.
783 (D) Quantification of the mNG-positive cell number in each field of view. Data are presented
784 as mean ± SEM. *p*-values were calculated using one-way ANOVA followed by Sidak's
785 multiple-comparison test for selected pairs. NS, $p \geqq 0.05$; †, $p < 0.05$. Sample size for each
786 condition is 4.
787

788 **Figure 2**

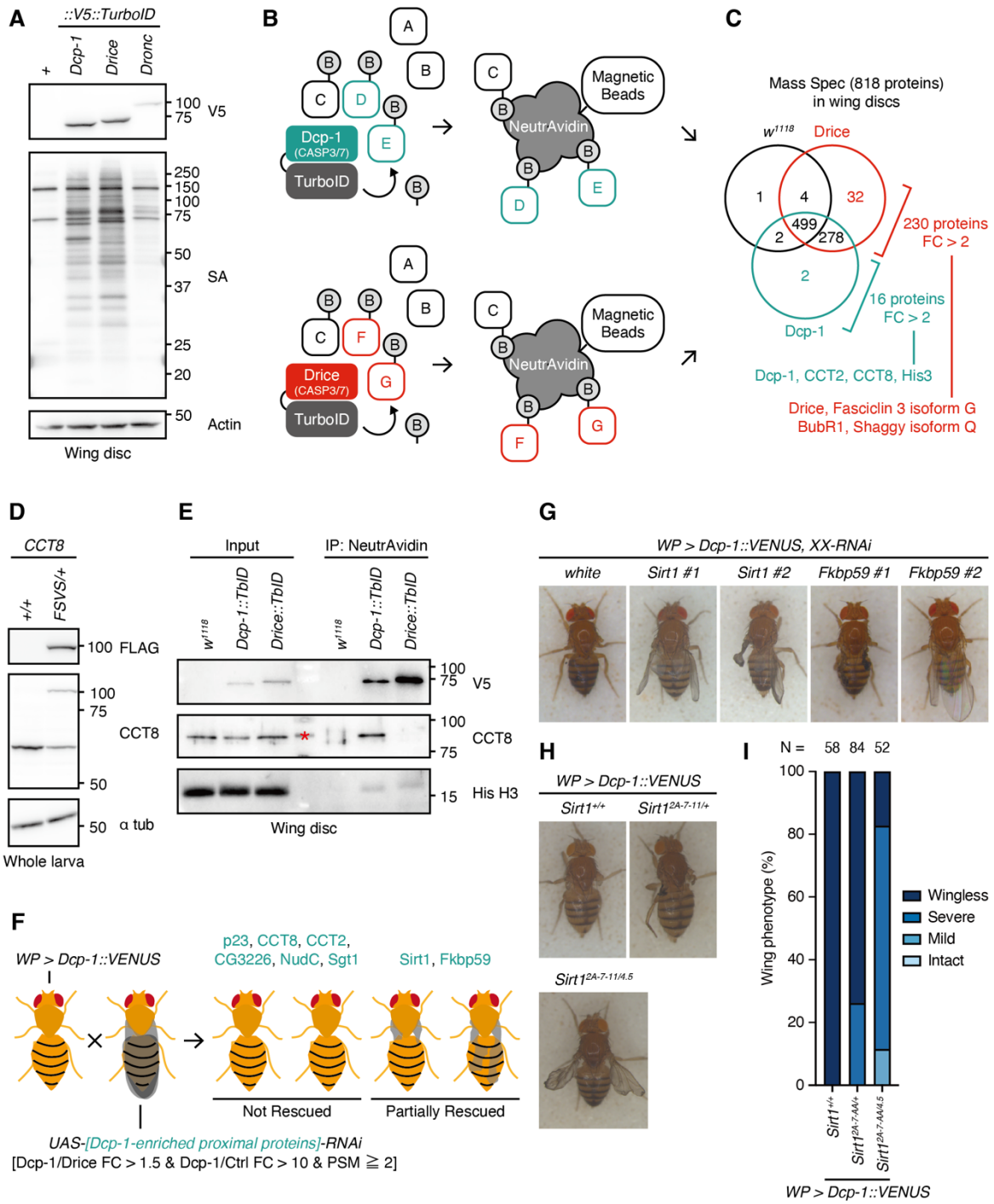

789
790

791 **Figure 2. Dcp-1-enriched proximal proteins are required for Dcp-1 activation.**
792 (A) Western blotting of expression of C-terminally V5::TurboID knocked-in tagged caspases
793 and biotinylation patterns of their proximal proteins detected by streptavidin (SA) in larval wing
794 imaginal discs.
795 (B) A schematic diagram of the TurboID-mediated identification of proximal proteins. Dcp-1-
796 and Drice-proximal proteins are promiscuously labeled in vivo with the administration of biotin.

797 Then, biotinylated proteins are purified using NeutrAvidin magnetic beads and are
798 subsequently analyzed by mass spectrometry.
799 (C) A summary of mass spectrometry analysis of proteins in the larval imaginal discs. Among
800 818 proteins identified, 230 proteins were detected as highly enriched proteins in
801 Drice::V5::TurboID flies (FC [Drice::V5::TurboID/Dcp-1::V5::TurboID] > 2) and 16 proteins
802 were detected as highly enriched proteins in Dcp-1::V5::TurboID flies flies (FC [Dcp-
803 1::V5::TurboID/Drice::V5::TurboID] > 2).
804 (D) Western blotting validation of the anti-CCT8 antibody in whole larval lysates without the
805 digestive tract and fat body. The anti-CCT8 antibody detects both endogenous CCT8 (MW:
806 59.4 kDa) and 3xFLAG::StrepII::VENUS::StrepII (FSVS)-tagged CCT8 (MW: 91.1 kDa).
807 (E) Western blotting of endogenous CCT8 expressed in larval wing imaginal disc. Dcp-1-
808 proximal and Drice-proximal proteins biotinylated by C-terminally knocked-in tagged
809 V5::TurboID are purified using NeutrAvidin. The red asterisk represents a non-specific band
810 in the marker lane.
811 (F) Schematic diagram of the RNAi screen targeting eight Dcp-1-enriched proximal proteins.
812 The *WP > Dcp-1::VENUS* line was crossed with each *UAS-RNAi* line, and wing phenotypes of
813 the F1 progeny were scored.
814 (G) Representative images of female wing phenotypes from *Dcp-1::VENUS* overexpression
815 driven by *WP-Gal4* with knockdown of Dcp-1-enriched proximal proteins. “XX” denotes the
816 knocked-down gene, and “#1” and “#2” indicate independent RNAi lines.
817 (H) Representative images of female wing phenotypes upon *Dcp-1::VENUS* overexpression
818 driven by *WP-Gal4* in the *Sirt1* null mutant background.
819 (I) Quantification of (H). Each wing is manually classified into four (wingless, severe, mild,
820 and intact) categories. Sample sizes are shown in the figure.
821

822 **Figure EV2**

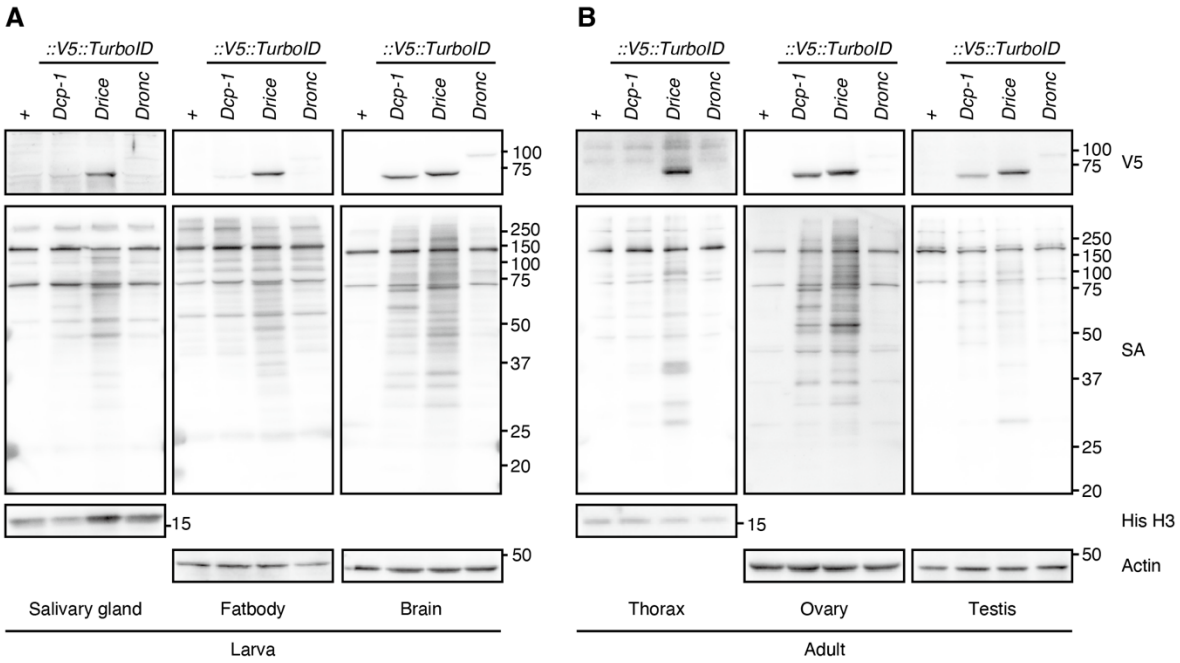

823
824

825 **Figure EV2. Expression patterns of *Drosophila* caspases in larval and adult tissues.**
826 (A) Western blotting of expression of C-terminally V5::TurboID knocked-in tagged caspases
827 and biotinylation patterns of their proximal proteins detected by streptavidin (SA) in larval
828 salivary gland, fat body, and brain.
829 (B) Western blotting of expression of C-terminally V5::TurboID knocked-in tagged caspases
830 and biotinylation patterns of their proximal proteins detected by SA in adult thorax, ovary, and
831 testis.
832

833 **Figure 3**

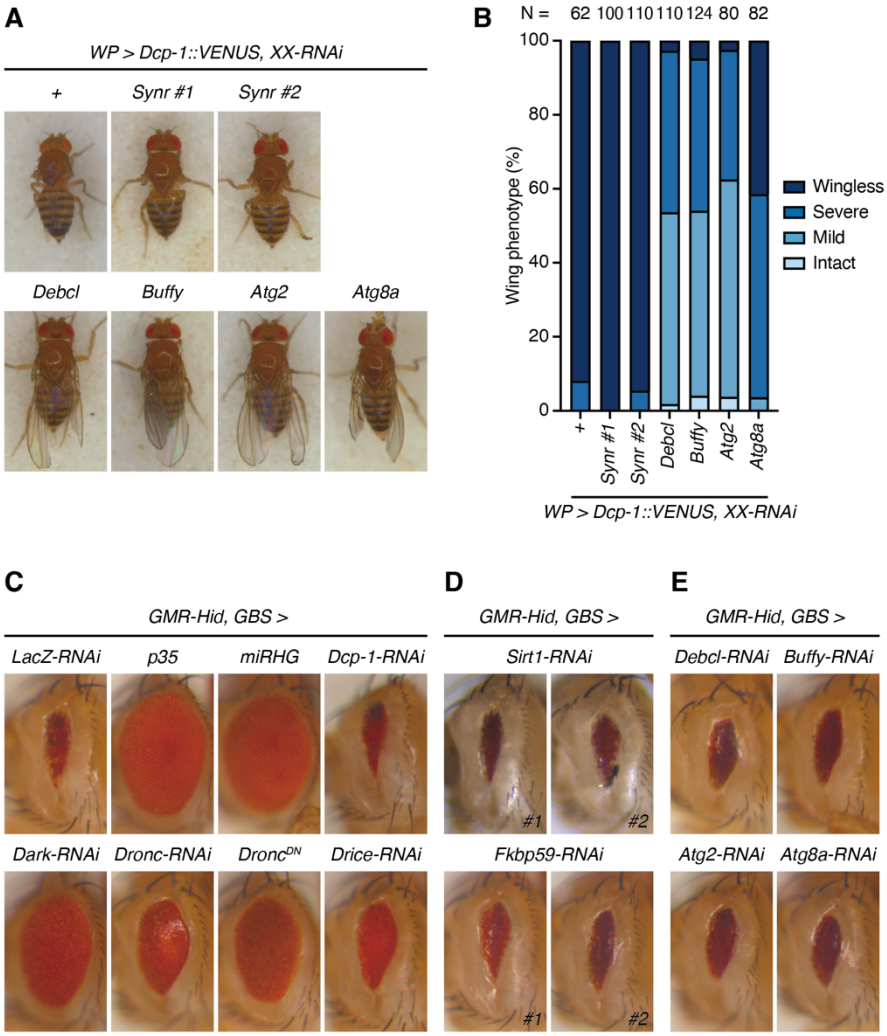

834
835
836 **Figure 3. Debcl, Buffy, and autophagy are specifically required for *Dcp-1* overexpression-**
837 **induced apoptosis.**
838 (A) Representative images of female wing phenotypes from *Dcp-1::VENUS* overexpression
839 driven by *WP-Gal4* with the genetic perturbation of *Synr*, *Debcl*, *Buffy,* and autophagy. "XX"
840 denotes the knocked-down gene, and "#1" and "#2" indicate independent RNAi lines.
841 (B) Quantification of (A). "XX" denotes the knocked-down gene, and "#1" and "#2" indicate
842 independent RNAi lines. Each wing is manually classified into four (wingless, severe, mild,
843 and intact) categories. Sample sizes are shown in the figure.
844 (C) Representative images of female eye phenotypes upon *Hid* overexpression with the genetic
845 perturbation of canonical apoptosis signaling.
846 (D) Representative images of female eye phenotypes upon *Hid* overexpression with the genetic
847 perturbation of *Sirt1* or *Fkbp59*. "#1" and "#2" indicate independent RNAi lines.
848 (E) Representative images of female eye phenotypes upon *Hid* overexpression with the genetic
849 perturbation of *Debcl*, *Buffy*, and autophagy.
850

851 **Figure EV3**

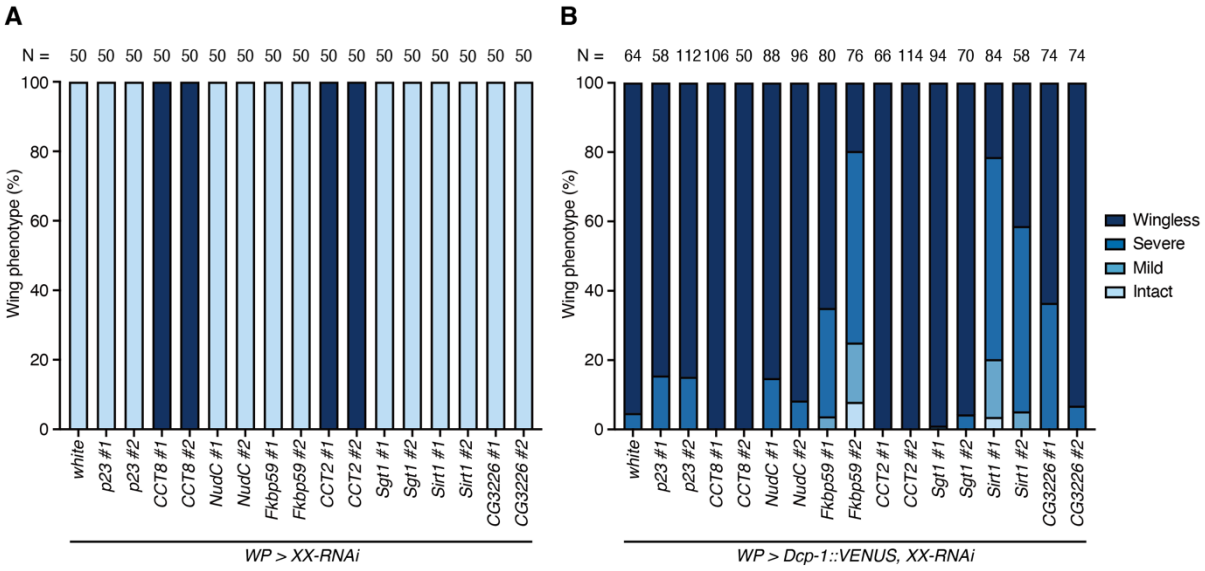

852
853
854 **Figure EV3. RNAi screening of Dcp-1-enriched proximal proteins for regulators of Dcp-**
855 **1 activation.**
856 (A) Quantification of female wing phenotypes upon knockdown of Dcp-1-enriched proximal
857 proteins driven by *WP-Gal4*. "XX" denotes the knocked-down gene, and "#1" and "#2" indicate
858 independent RNAi lines. Each wing is manually classified into four (wingless, severe, mild,
859 and intact) categories. Sample sizes are shown in the figure.
860 (B) Quantification of female wing phenotypes upon *Dcp-1::VENUS* overexpression driven by
861 *WP-Gal4* with simultaneous knockdown of Dcp-1-enriched proximal proteins. "XX" denotes
862 the knocked-down gene, and "#1" and "#2" indicate independent RNAi lines. Each wing is
863 manually classified into four (wingless, severe, mild, and intact) categories. Sample sizes are
864 shown in the figure.
865

866 **Figure 4**

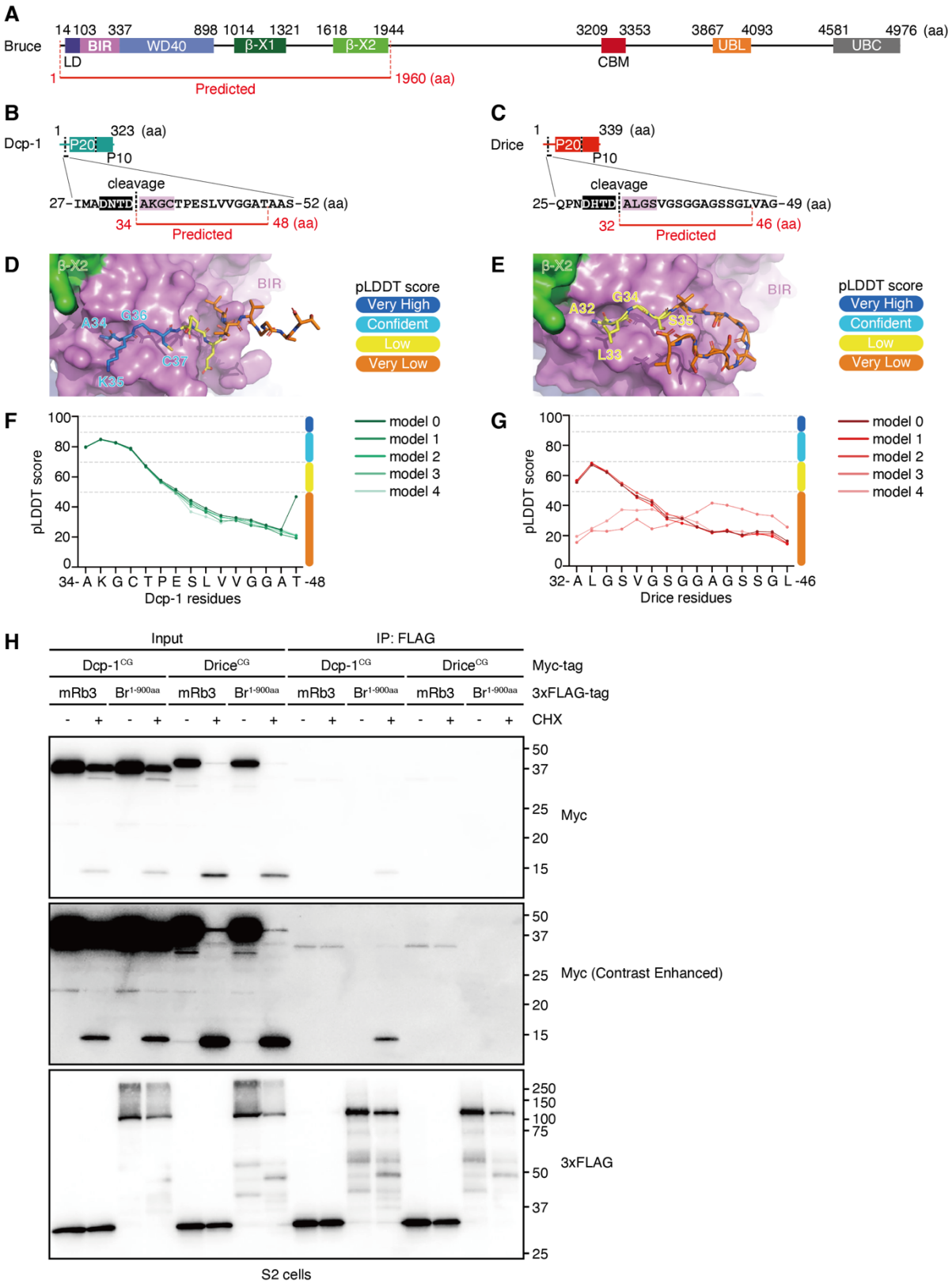

867

868 **Figure 4. Cleaved Dcp-1, but not Drice, interacts with Bruce.**

869 (A) Domain structure of Bruce. LD denotes the linker domain, WD40 a WD40 domain, BIR
870 the Baculoviral IAP repeat, β-X a β-sandwich-like fold, CBM a domain resembling the

carbohydrate-binding module family 32 (CBM), UBL the ubiquitin-like domain, and UBC the E2-E3 hybrid ubiquitin-conjugating (UBC) domain. The region used for structural prediction using AlphaFold3 is indicated in red.

(B) IBM-like sequence in Dcp-1. The propeptide cleavage site of Dcp-1 is indicated by a black dashed line; the caspase recognition motif is highlighted in black; the IBM-like sequence is highlighted in pink; and the region used for AlphaFold3 prediction is shown in red.

(C) IBM-like sequence in Drice. The propeptide cleavage site of Drice is indicated by a black dashed line; the caspase recognition motif is highlighted in black; the IBM-like sequence is highlighted in pink; and the region used for AlphaFold3 prediction is shown in red.

(D) Predicted complex structure of Bruce BIR and Dcp-1 IBM-like sequence. The AlphaFold3 prediction [model 0] is shown. The Bruce β-X2 and BIR domains are displayed as surfaces in green and pink, respectively. Dcp-1 is shown in stick representation and color-coded according to pLDDT scores, as indicated in the figure. See also panel (F).

(E) Predicted complex structure of Bruce BIR and Drice IBM-like sequence. The AlphaFold3 prediction [model 0] is shown. The Bruce β-X2 and BIR domains are displayed as surfaces in green and pink, respectively. Drice is shown in stick representation and color-coded according to pLDDT scores, as indicated in the figure. See also panel (G).

(F) pLDDT scores of Dcp-1 in the five predicted complex structures with Bruce. For all five AlphaFold3 models, per-residue pLDDT scores of Dcp-1 are plotted. Prediction confidence is color-coded as follows: very high (pLDDT > 90) in dark blue, confident (90 > pLDDT > 70) in light blue, low (70 > pLDDT > 50) in yellow, and very low (pLDDT < 50) in orange.

(G) pLDDT scores of Drice in the five predicted complex structures with dBruce. For all five AlphaFold3 models, per-residue pLDDT scores of Drice are plotted. Prediction confidence is color-coded as follows: very high (pLDDT > 90) in dark blue, confident (90 > pLDDT > 70) in light blue, low (70 > pLDDT > 50) in yellow, and very low (pLDDT < 50) in orange.

(H) Co-immunoprecipitation of N-terminally 3xFLAG-tagged N-terminal region of Bruce (Br, 1–900 aa; containing LD, BIR, and WD40 domains) with C-terminally myc-tagged, catalytically inactive Dcp-1 or Drice (catalytic cysteine mutated to glycine; CG) expressed in *Drosophila* S2 cells. N-terminally 3xFLAG-tagged mRuby3 (mRb3) was used as a control. Apoptosis was induced by cycloheximide (CHX) treatment. 3xFLAG-tagged proteins were immunoprecipitated using an anti-3xFLAG antibody.

903 **Figure EV4**

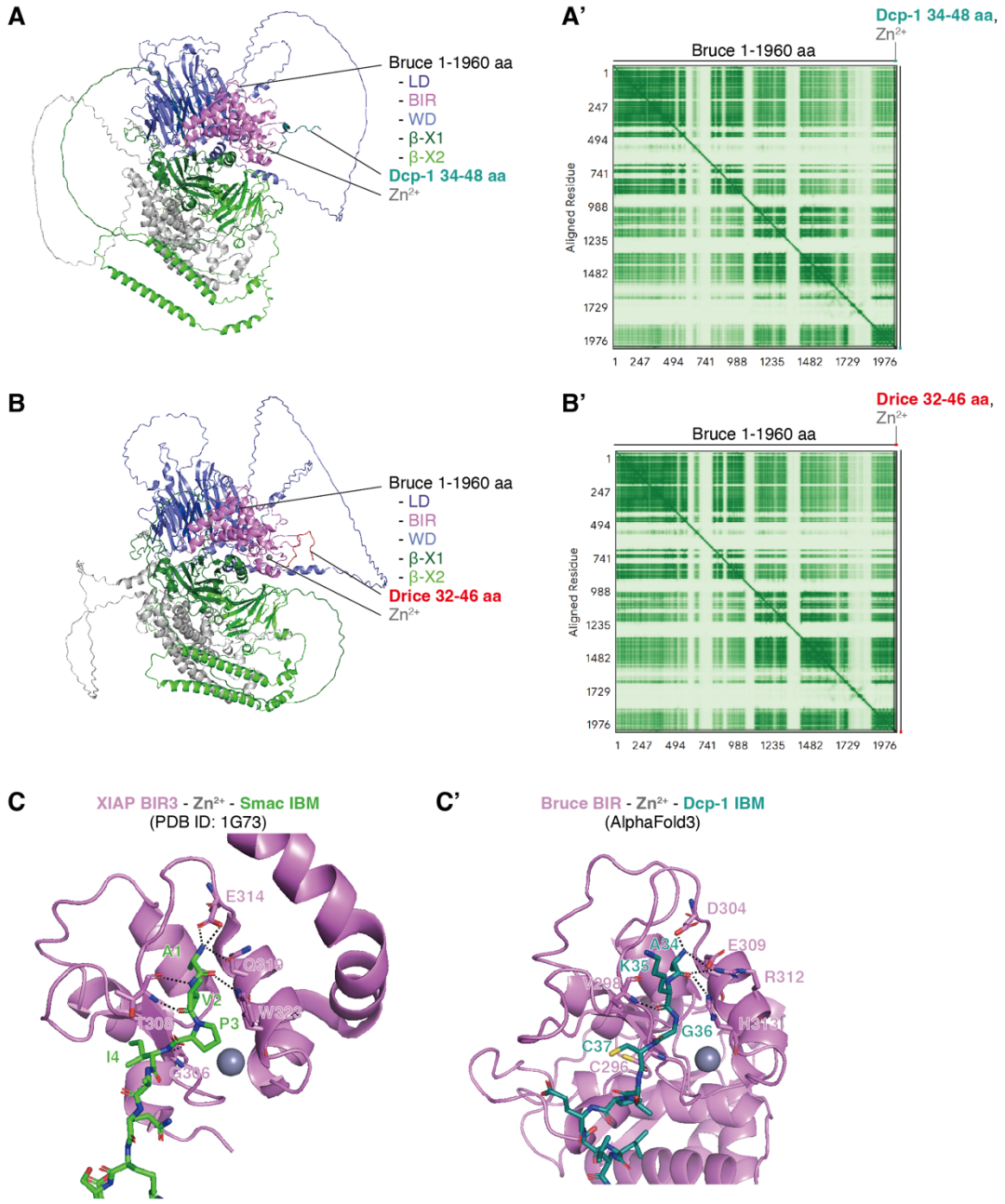

904
905

906 **Figure EV4. Predicted structures of Bruce complexed with Dcp-1 and Drice IBM-like**
907 **sequences.**
908 (A) Overall view of the predicted complex structure of Bruce and Dcp-1. Model 0 is shown
909 with the same color scheme as in Figure 4A and B. The predicted position error is shown in
910 (A').
911 (B) Overall view of the predicted complex structure of Bruce and Drice. Model 0 is shown with
912 the same color scheme as in Fig. 4A and C. The predicted position error is shown in (B').
913 (C) Structural comparison between the experimentally determined complex of XIAP BIR3 and
914 Smac IBM (C), and the predicted complex of dBruce BIR and Dcp-1 IBM (C'). XIAP BIR3 is
915 shown as a pink cartoon and the Smac IBM as green sticks (PDB ID: 1G73, right panel). dBruce

916 BIR domain is shown as a pink cartoon and the Dcp-1 IBM as dark green sticks (model 0, left
917 panel). Zn^{2+} ions are shown as gray spheres. Salt bridges are indicated by black dashed lines,
918 along with the corresponding interacting residues.
919

920 **Figure 5**

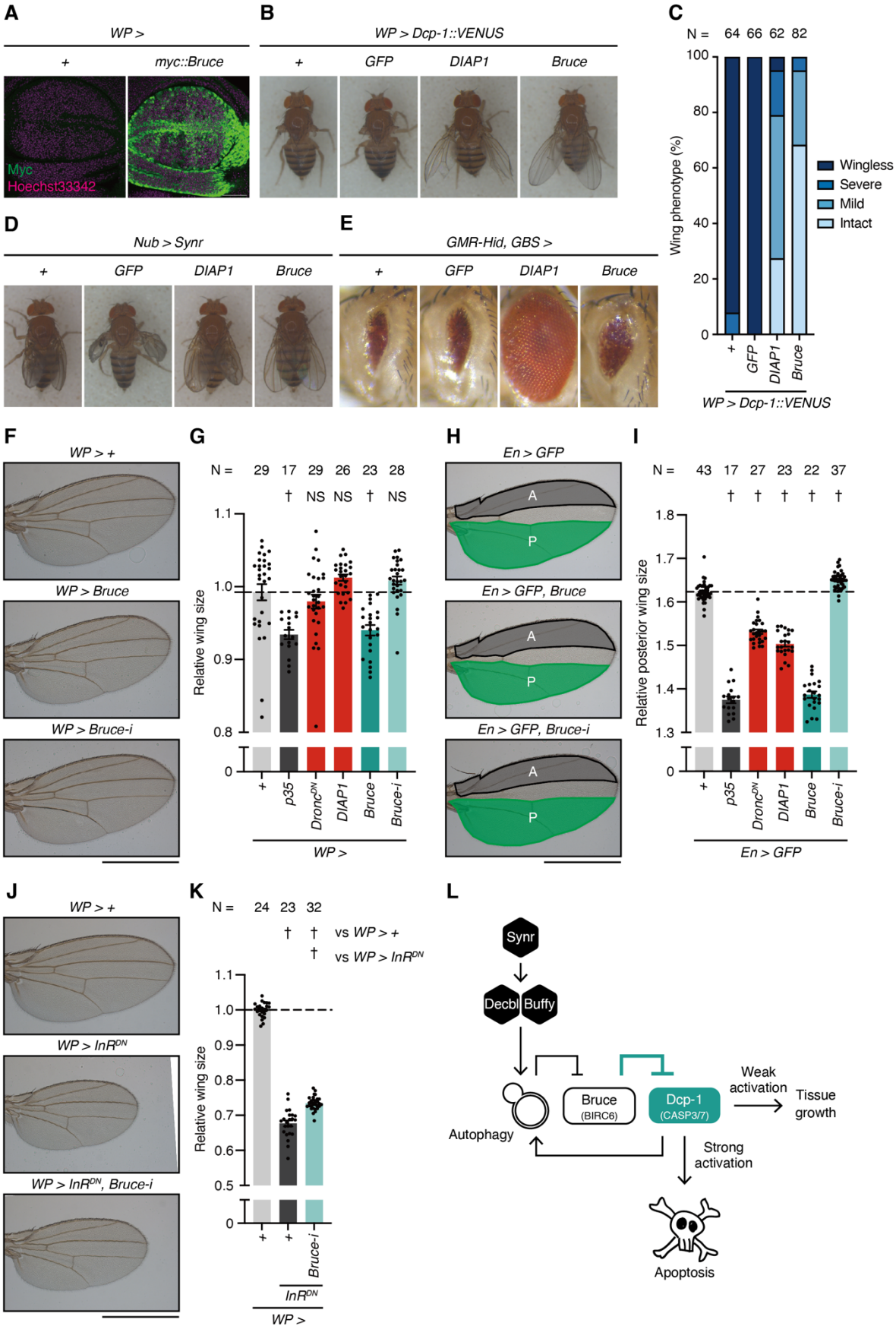

921

Figure 5. Bruce selectively suppresses Dcp-1 activity and wing tissue growth.

(A) Expression pattern of overexpressed *myc::Bruce* (green) by using *WP-Gal4* in the wing imaginal discs. Nuclei are visualized using Hoechst 33342 (magenta). Scale bar: 50 μm.

(B) Representative images of female wing phenotypes from *Dcp-1::VENUS* overexpression driven by *WP-Gal4* with *DIAP1* or *Bruce* overexpression.

(C) Quantification of (B). Each wing is manually classified into four (wingless, severe, mild, and intact) categories. Sample sizes are shown in the figure.

(D) Representative images of female wing phenotypes upon *Synr* overexpression driven by *Nub-Gal4* with *DIAP1* or *Bruce* overexpression.

(E) Representative images of female eye phenotypes upon *Hid* overexpression with *DIAP1* or *Bruce* overexpression.

(F) Representative images of female wing upon *Bruce* or *Bruce-RNAi* (*Bruce-i*) overexpression using *WP-Gal4*. Scale bar: 1 mm.

(G) Quantification of relative wing size normalized to the corresponding *No-Gal4* control. Data are presented as mean ± SEM. *p*-values were calculated using one-way analysis of variance (ANOVA) followed by Dunnett's multiple-comparison test against no UAS control. NS, $p \geqq 0.05$; †, $p < 0.05$. Sample sizes are shown in the figure.

(H) Representative images of female wing upon *Bruce* or *Bruce-RNAi* (*Bruce-i*) overexpression using *En-Gal4*. The grey area (labelled as A) represents the anterior part, and the green area (labelled as P) represents the posterior part of the wing. Scale bar: 1 mm.

(I) Quantification of relative posterior part of wing size normalized to corresponding anterior part of wing size. Data are presented as mean ± SEM. *p*-values were calculated using one-way ANOVA followed by Dunnett's multiple comparison test against no UAS control. †, $p < 0.05$. Sample sizes are shown in the figure.

(J) Representative images of female wing upon InR^{DN} and *Bruce-RNAi* (*Bruce-i*) overexpression using *WP-Gal4*. Scale bar: 1 mm.

(K) Quantification of relative wing size normalized to control (*WP* > +). Data are presented as mean ± SEM. p-values were calculated using one-way ANOVA followed by Sidak's multiple comparison test for selected pairs.†, $p < 0.05$. Sample sizes are shown in the figure.

(L) Schematic diagram of Dcp-1 activity-regulating alternative apoptosis signaling pathway in *Drosophila* mediated by autophagy-Bruce axis.

954 **Figure EV5**

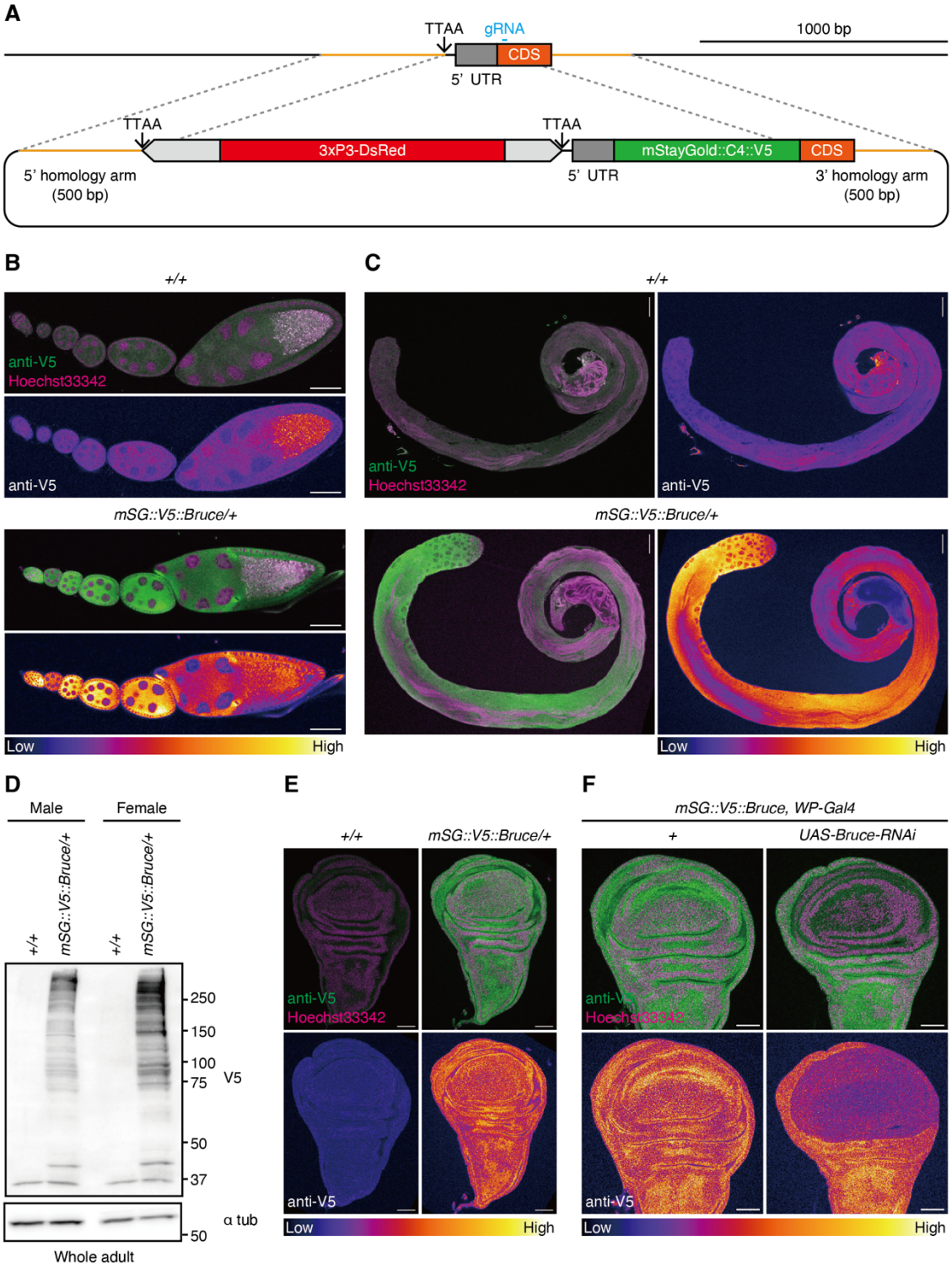

955
956

957 **Figure EV5. Expression patterns of mStayGold::V5-tag knocked-in Bruce.**
958 (A) Schematic diagram of CRISPR/Cas9-mediated knock-in of mStayGold::C4 linker (C4)::V5
959 tag at the N-terminus of Bruce. A 3xP3-DsRed cassette was integrated at the endogenous TTAA
960 site as a transformation marker. Removal of the cassette restores the genomic TTAA site,
961 enabling scarless genome engineering.

962 (B) Expression pattern of mStayGold (mSG)::C4::V5-tag knocked-in Bruce (green) in the
963 ovariole. Nuclei are visualized using Hoechst 33342 (magenta). Scale bar: 50 µm.
964 (C) Expression pattern of mSG::C4::V5-tag knocked-in Bruce (green) in the testis. Nuclei are
965 visualized using Hoechst 33342 (magenta). Scale bar: 50 µm.
966 (D) Western blotting of expression of mSG::C4::V5-tag knocked-in tagged Bruce in the whole
967 adult male and female.
968 (E) Expression pattern of mSG::C4::V5-tag knocked-in tagged Bruce (green) in the wing
969 imaginal discs. Nuclei are visualized using Hoechst 33342 (magenta). Scale bar: 50 µm.
970 (F) Expression pattern of mSG::C4::V5-tag knocked-in tagged Bruce (green) in the wing
971 imaginal discs upon *Bruce-RNAi* using *WP-Gal4*. Nuclei are visualized using Hoechst 33342
972 (magenta). Scale bar: 50 µm.
973

974 **Legends for Tables**
975
976 **Table EV1. Dcp-1 and Drice proximal protein lists.**
977 Lists of the identified Dcp-1 proximal proteins (abundance ratio (Dcp-
978 1::V5::TurboID/Drice::V5::TurboID) > 2), Drice proximal proteins (abundance ratio
979 (Drice::V5::TurboID/Dcp-1::V5::TurboID) > 2), and candidates for RNAi screening
980 (abundance ratio (Dcp-1::V5::TurboID/Drice::V5::TurboID) > 1.5, abundance ratio (Dcp-
981 1::V5::TurboID/Control) > 10, PSM ≧ 2). The UniProt accessions, gene description,
982 abundance ratio, and # PSMs are listed.
983
984 **Table EV2. Fly stock list.**
985 List of fly strains. Genotypes, maps, source or references, and stock numbers are listed.
986
987 **Table EV3. Detailed genotypes.**
988 Detailed genotypes and their related figure # are presented.
989
990 **Table EV4. Liquid chromatography (LC) settings.**
991 Gradient settings for LC analysis are presented.
992
993 **Table EV5. Tandem mass spectrometry (MS/MS) settings.**
994 Settings used for the MS/MS analysis are presented.
995
996 **Table EV6. Proteome Discoverer 2.2 settings.**
997 Proteome Discoverer 2.2 settings for proteomics analysis are presented.
998